Ocean Modelling 186 (2023) 102276

Contents lists available at ScienceDirect

Ocean Modelling

journal homepage: www.elsevier.com/locate/ocemod

Seasonal dynamics of water circulation and exchange flows in a shallow lagoon-inlet-coastal ocean system☆

Miaohua Mao [a,b,c], Meng Xia [c,*]

[a] CAS Key Laboratory of Coastal Environmental Processes and Ecological Remediation, Yantai Institute of Coastal Zone Research, Chinese Academy of Sciences, Yantai, Shandong 264003, PR China
[b] Shandong Key Laboratory of Coastal Environmental Processes, Yantai, Shandong 264003, PR China
[c] Department of Natural Sciences, University of Maryland Eastern Shore, Princess Anne, MD 21853, USA

ARTICLE INFO

Keywords:
Seasonal dynamics
Shallow lagoonal system
Winds
Tides
Numerical modeling

ABSTRACT

A wave–current coupled, unstructured-grid, three-dimensional hydrodynamic model was applied to investigate the seasonal dynamics of the Maryland Coastal Bays system. The model's performance was validated successfully against hydrodynamic observations from the spring to fall of 2014, and the driving forces of water circulation and exchange flows were discussed. Results indicate that seasonal dynamics are primarily controlled by tides, modulated by winds, waves, and density variations, and regulated by the inlet orientation and geometry. Seasonal circulation in the surface layer is stronger than that near the bottom. The strong coastal circulation, net outflows via inlets, and the clockwise movements in the southern Isle of Wight Bay are primarily controlled by tides. The directional alignment between winds and the bay's principal axis and inlet orientation are key to the seasonal circulation and exchange flows in Sinepuxent Bay and via inlets. Wave-induced effects are comparable to tides in particular regions (e.g., reaching 30 cm/s in Isle of Wight Bay), and much larger than those caused by density variations overall. Additional numerical experiments indicate that spatial variations in salinity are mainly responsible for the density-induced circulation (e.g., 6 cm/s at the mouth of Newport River in Newport Bay). Further analysis indicates that the net exchange flows vary from the surface to bottom layers (e.g., different magnitudes or transporting directions) both in the lagoon and via the paired inlets. This work is beneficial to coastal communities and numerical modelers in understanding the dynamics of shallow lagoon-inlet-coastal ocean systems at a seasonal timescale.

1. Introduction

In a lagoonal system, water circulation and exchange flows determine residence time (Cucco et al., 2009), salt fluxes (Lerczal amd Geyer, 2006), and nutrient/pollutant exchanges with the adjacent coastal ocean, which subsequently impact the water quality (Ouillon et al., 2010; Defne and Ganju, 2015), larval retention (Cuif et al., 2014) and particle fate (Xia et al., 2011b; Beudin et al., 2017). Therefore, a comprehensive understanding of the physical dynamics is fundamental for making informed management decisions (Tsihrintzis et al., 2007; García-Oliva et al., 2018). Stretching over the land–coastal ocean interface, the highly dynamic and shallow lagoon-inlet-coastal ocean system has been studied intensively, both along the European coasts (e.g., the western Dutch Wadden Sea, Netherlands (Duran-Matute et al., 2016) and the Ria Formosa Lagoon, Portugal (Fabião et al., 2016)) and the U.S. East and Gulf Coasts, including Perdido Bay (Xia et al., 2011a), Indian River Lagoon, Florida (Weaver et al., 2016), and Galveston Bay, Texas (Salas-Monreal et al., 2018).

Water circulation and exchange flows in lagoonal/estuarine/bay systems are synergistically controlled by wind forcing, astronomical tides, baroclinic processes, and surface gravity waves (Smith, 2001; Valle-Levinson and Blanco, 2004; Buijsman and Ridderinkhof, 2007; Mohanty and Panda, 2009; Chou et al., 2015; Salles et al., 2015). Smith (2001) found that seasonal variations in winds have substantial impacts on water flows and exchanging fluxes in a multiple-inlet lagoon along the Atlantic coast of Florida. Using an analytical model, Buijsman and Ridderinkhof (2007) indicated that water flows and exchanges in the western Wadden Sea are dictated by the wind direction under strong

☆ Ocean Modelling (Minor Revision: 10/05/2023)

* Corresponding author.
E-mail address: mxia@umes.edu (M. Xia).

https://doi.org/10.1016/j.ocemod.2023.102276
Received 28 April 2023; Received in revised form 10 October 2023; Accepted 10 October 2023
Available online 12 October 2023

weather conditions. Subsequently, Salles et al. (2015) noted that seaward winds significantly enhance (reduce) inflows (outflows) in the South (North) Pass of the Arcachon Lagoon, France. Considering the spatial variations in water temperature and salinities, Mohanty and Panda (2009) stated that the density gradient induced currents are primarily responsible for the seasonal exchanges between the outer channel and central sector of the Chilika Lagoon, India. Although a series of studies have provided encouraging insights into the forcing mechanism of water movements and exchanging dynamics, the contributions of waves to the mean circulation and exchange flows have been barely addressed, both in the bay (Lu et al., 2021; Song et al., 2021) and in the shallow lagoonal system (Olabarrieta et al., 2011; Dodet et al., 2013; Wargula et al., 2018; Lavaud et al., 2020).

The Maryland Coastal Bays system (MCBs) is a typical shallow lagoon-inlet-coastal system, experiences physical processes that substantially affect local fish recruitment (Love et al., 2009), water quality, and biodiversity (Boynton et al., 1996; Jesien et al., 2009). Nevertheless, comprehensive discussions on the characteristics and dynamics of water circulation and exchanges have yet to be conducted since the pioneering work of Pritchard (1960). After about half a century, Wang et al. (2013) applied a numerical model for the MCBs, briefly describing the water circulation near the inlet during several semidiurnal tidal periods. Recently, the physical dynamics have been investigated over the entire domain of the MCBs (e.g., including the paired inlets, lagoon, and adjacent coastal ocean) under complex external conditions (e.g., the combined effects of winds and tides). Based on the wind climatology data spanning from 2003 to 2013, Kang et al. (2017) designed several numerical experiments using spatially uniform and constant winds (e.g., southwesterly/northwesterly representing summer/winter season) and determined that both tidally and wind-driven currents are critical to the water circulation and exchanges in the MCBs. They further stated that the relative contributions of winds (e.g., intensity and direction) and tides to the water circulation and exchanges depend upon the wind intensity when winds are strong, and tides are relatively weak.

Using a wave–current coupled model, Beudin et al. (2017) and Mao and Xia (2018) suggested that waves play substantial roles in this shallow lagoon-inlet-coastal ocean system during extreme events. Given that biogeochemical processes that dictate ecosystem health occur over seasonal or climatological scales, understanding the seasonal dynamics of lagoon-type estuaries is an important aspect of ecosystem health and sustainability. However, modeling long-term hydrodynamics in lagoonal or estuarine systems is generally challenging due to the absence of a dominant physical process that clearly governs these dynamics. For example, tides dictate the dynamics in macro tidal, well-mixed estuaries while the baroclinic circulation is more important in relatively deeper, partially stratified ones. Because of the difficulty in simulating these long-term processes, it is particularly challenging to assess the role that various processes play in the water circulation and exchange flows of the MCBs. In many cases the modeling errors may exceed the value in the circulation and flux attributable to a specific process.

This study aims to explore the relative contributions of winds, tides, baroclinic processes, and waves to the seasonal circulation and exchange flows in the MCBs by using a state-of-the-art, unstructured-grid, three-dimensional, wave–current coupled, high-resolution and accuracy model of Mao and Xia (2018). The issues to be solved include (1) seasonal characteristics of the spatial distributions of the water circulation and exchange flows with the coastal ocean, (2) relative effects of winds versus tides, and (3) contributions of baroclinic processes and short waves over various regions of this system. Answering these scientific questions will enhance our understanding of the fundamental dynamics over the large spatial extent of the entire lagoon-inlet-coastal ocean system at a long-term timescale. Data from sixteen hydrodynamic and two wind observational stations were collected and compared from spring to fall in 2014 to examine the model performance over wide spatial coverages and long timescales. The remaining sections of this paper are organized as follows. Section 2 introduces the methodology, which includes the model description, data sources, numerical experiments, and skill metrics; Section 3 shows the model skill assessment and numerical results; Section 4 discusses the relative effects of local winds, tides, baroclinic processes, and waves on the seasonal circulation and exchange flows; Section 5 presents the major conclusions.

2. Methodology

2.1. Model description and study domain

This study applies a free surface, three-dimensional (3D), primitive equation-based Finite-Volume Community Ocean Model (FVCOM) (Chen et al., 2013) to the MCBs, which adopts a second-order, upwind finite-volume method and a modified, explicit fourth order Runge–Kutta time-stepping scheme for the advection and time integration, respectively. The modified MY-2.5 model (Galperin et al., 1988) and eddy parameterization scheme (Smagorinsky, 1963) are used to handle the vertical and horizontal mixing processes, respectively. The hydrostatic approximation is made so that the pressure at any point in the ocean is due to the weight of water above it. Boussinesq assumptions are utilized, which means density variations are neglected except for the term multiplied by gravity acceleration in the buoyance force. Based on the Courant–Friedrich–Lewy criterion for numerical stability, a short time step of 1 s is set. The net surface heat flux is calculated by including the wind speed, air temperature, relative humidity, downward shortwave, and upward longwave radiation fluxes (Fairall et al., 1996). The surface wave model (SWAVE) (Qi et al., 2009) is based on the wave action equation, which considers local and spatial variations, depth and current-induced wave refraction and frequency shift, wind input, nonlinear wave–wave interactions, whitecapping, bottom friction, and depth-induced wave breaking. The model solves the wave spectral frequency in the 0.05–0.5 Hz range with 10 bins. A full sector of wave directions (i.e., 0–360°) with 18 bins (e.g., each of 20°) is applied. Time step for wave calculations is 10 s, identical to the time interval of the wave–current coupling process. The coupled FVCOM/SWAVE system allows for the computation of wave breaking, refraction, and frequency shift in the SWAVE wave model with the inclusion of water depth and current variations. Simultaneously, wave-induced 3D radiation stress (Mellor, 2015), wave-altered bottom friction stress (Soulsby, 1997), and sea surface roughness (Donelan et al., 1993) are incorporated into the FVCOM circulation model. In addition, wave-induced vertical mixing and turbulence are account for the short-wave effects on the mean circulation. The version of the wave-current model applied in this study is advanced compared to the state of the art. For example, this study incorporates the recently developed 3D radiation stress theory by Mellor (2015) that addresses issues in previous versions (Mellor, 2003; 2005; 2008) by correcting the improper treatment of the pressure term and rectifying the unrealistic, surface intensified force in the vertical flux term.

The study domain of the MCBs (Fig. 1a) includes Assawoman Bay (AB) and Isle of Wight Bay (IWB) as upper bays, Sinepuxent Bay (SB), Newport Bay (NB), and Chincoteague Bay (CB) as lower bays, and Ocean City Inlet (OCI) and Chincoteague Inlet (CI) as tidal inlets. The width and length of the OCI are 0.2–0.4 km by 1 km, while they are 1 km and 3 km for the larger CI, respectively. The principal axis of the MCBs follows a southwest–northeast direction, nearly perpendicular and parallel to the orientations of OCI and CI, respectively. Water depths of the shallow lagoon are mostly below 2 m, except for the navigation channels within the inlets (e.g., 7–10 m). For brevity, the coastal ocean in this study refers to the coastal zone seaward of the lagoon along Fenwick Island (FI), Assateague Island (AI), and Wallops Island (WI) within the 10-m isobath. To resolve the highly variable bathymetry and complex geometry near coasts and around islands, the unstructured triangular mesh is employed in horizontal with 7332 nodes and 12,428 elements. Grid sizes are less than 10 m in the shallow water regions and gradually increase up to 1.74 km along the deep open boundary layer. Given that the

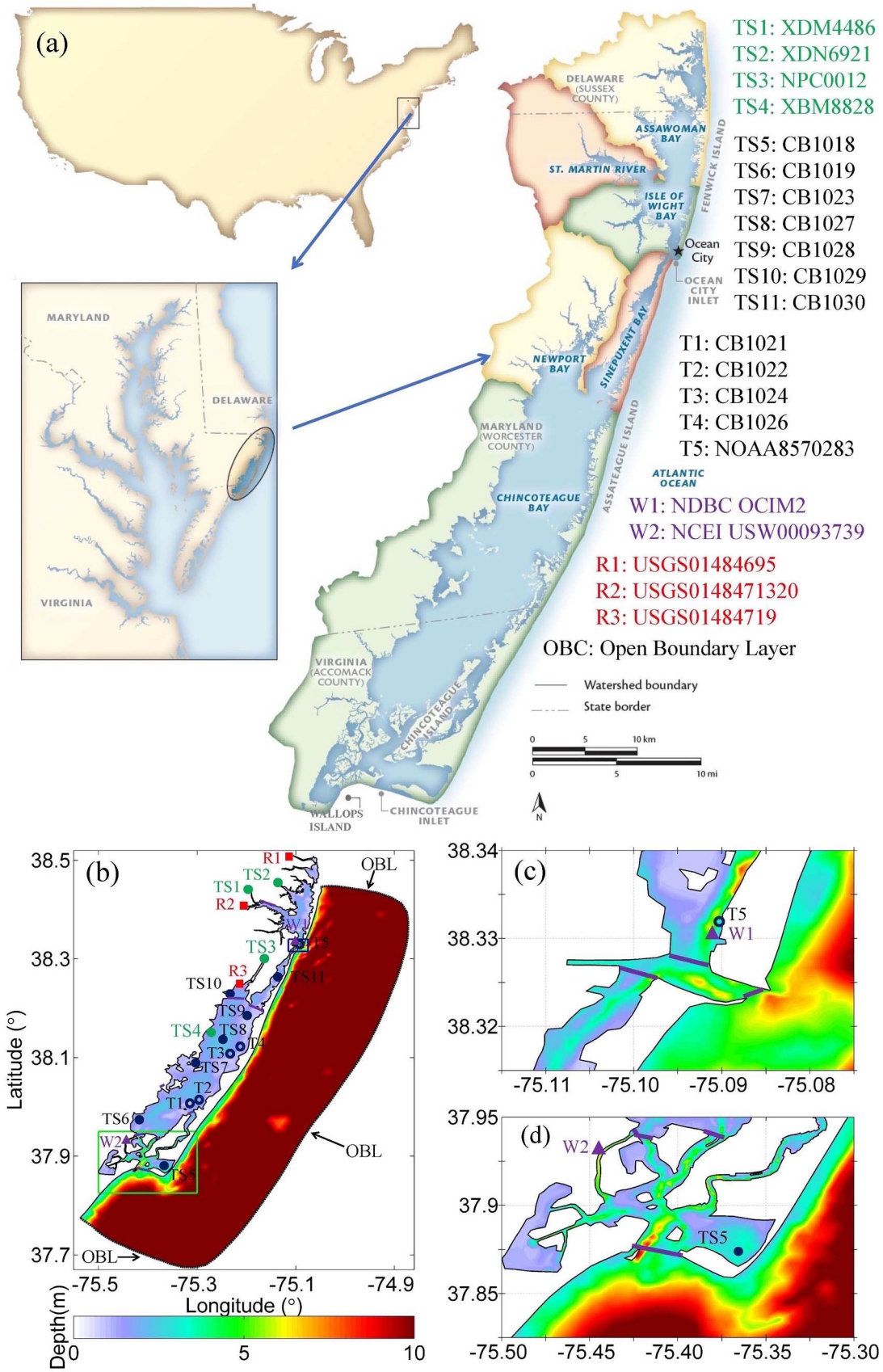

Fig. 1. (a) Geographic location of the MCBs; (b) bathymetry of the MCBs and locations of observed stations and enlarged maps for the (c) OCI in blue box and (d) CI in green box. Filled circles: water temperature and salinity stations from the (green) MD department of Natural Resources and (blue) USGS; open circles: water temperature from the USGS; red squares: river inputs from the USGS; purple triangles: wind data from the (W1) NDBC, (W2) USGS, and (W3) NCEI; purple solid lines: borders among the sub-bays, inlets, and coastal ocean.

hydrodynamic and wave simulations have been proven satisfactory with the usage of five sigma layers (Kang et al., 2017; Mao and Xia, 2018; Kang and Xia, 2022), and the same setting for the vertical coordinate was adopted herein.

2.2. Model inputs and observations

Model inputs of atmospheric variables, which have a spatial resolution of 32-km and a time interval of 6 h, were derived from the National Centers for Environmental Prediction's (NCEP) North American Regional Reanalysis (NARR, www.esrl.noaa.gov/psd/data/narr). Wind quality from the NARR was examined against observations from the National Data Buoy Center's (NDBC) OCIM2 (http://www.ndbc.noaa.gov) near OCI and National Centers for Environmental Information's (NCEI) USW00093739 (https://www.ncdc.noaa.gov) near CI (Fig. 1b). Water temperature and salinities along the open boundary layer were processed according to the 3-km spatial and 3-h temporal outputs of the global Navy Coastal Ocean Model (https://www.ncdc.noaa.gov/data-access/model-data/model-datasets/navoceano-ncom-reg). Hourly water surface elevations along the open boundary layer were interpolated from the National Oceanic and Atmospheric Administration's (NOAA) tide gage data (http://tidesandcurrents.noaa.gov) at Ocean City, Maryland (38.328°N, 75.091°W) and Wachapreague, Virginia (37.608°N, 75.686°W). Wave parameters (e.g., significant wave height, peak wave period, and mean wave direction) nested along the open boundary layer were derived from the 0.09° × 0.09° gridded data of the Wave Information Studies Wave Model (Hubertz, 1992) maintained by the U.S. Army Corps of Engineers for the U.S. Atlantic East Coast (http://wis.usace.army.mil/hindcasts.html?dmn=atlantic). The parametric spectral input of the JONSWAP (Hasslemann et al., 1973) was used herein. Applications of more realistic types of wave spectra may reduce model errors in simulations of surface gravity waves (Xu and Yu, 2020) and wave-induced processes (Wargula et al., 2018), but it is beyond the scope of this work. Station NOAA8570283 near OCI provided hourly bottom water temperature. The United States Geological Survey (USGS) provided eleven and four stations for water temperature and salinity observations, respectively. Four additional sites were provided by Ms. C. Wazniak of the Maryland Department of Natural Resources Tidewater Ecosystem Assessment Division (http://eyesonthebay.dnr.maryland.gov). Detailed information on the observations is referred in Fig. 1 and Table 1.

2.3. Study periods and model experiments

Given that the wave–current coupled model applied to the MCBs had proved satisfactory skill in simulating water surface elevations, 3D current velocities, and wave parameters from the surf zone to the coastal ocean in Mao and Xia (2018), this work further validated the hydrodynamic model with the help of additional variables including 3D water temperature and salinities. Considering that the MCBs in winter is impacted by the ice formation (Ganju et al., 2017), this study focused on the dynamics of water circulation and exchange flows during the ice-free period. Therefore, numerical experiments were conducted in the spring (March–May), summer (June–August), and fall (September–November) of 2014. Additional runs were included by individually switching off winds, tides, baroclinic processes, and waves in the standard model. To understand lagoon–inlet–coastal ocean water exchanges at a seasonal timescale, the depth-integrated water transport flux, simply known as the instantaneous volume flux, which is often referred to as the flux Q, across the specified transect was calculated:

$$Q = \int_{-h}^{\eta}\int_{x_1}^{x_2} \vec{v}(x,z)\cdot\hat{n}\,dx\,dz, \tag{1}$$

where dx is the width of the computational element in the x-direction, and dz is the height of intra-sigma levels in the z-direction; $\vec{v}(x,z)$ represents the current vector, and $\hat{n}$ is the unit vector normal to the projected transect. The integration of each transect is taken from x_1 to x_2 in the horizontal and dz throughout the water column. The flux Q is defined as positive in the northward or eastward direction, and it is defined as negative in the southward or westward direction. The surface, middle and bottom currents refer to the flows in the 1st, 3rd, and 5th sigma layers of the water column counted from the surface layer. Time-averaging this volume flux Q, which we denote as $\langle Q \rangle$, gives the sum of

Table 1
Geographic information for the observational stations, and *CC, RB* and *RMSD* for water temperature and salinities from March 1 to November 30, 2014.

Variable	Station	Long. (°)	Lat. (°)	Depth (m)	*CC*	*RMSD* (°C)
Water temperature	CB1018	–75.3683	37.8670	3.0	0.95	1.3
	CB1019	–75.3961	37.9813	2.3	0.99	0.7
	CB1021	–75.3096	38.0100	0.8	0.98	2.0
	CB1022	–75.3081	38.0118	1.1	0.99	1.8
	CB1023	–75.2831	38.0914	1.9	0.99	1.1
	CB1024	–75.2524	38.0901	0.9	0.98	1.2
	CB1026	–75.2500	38.0983	1.2	0.99	2.1
	CB1027	–75.2380	38.1493	2.2	0.97	1.2
	CB1028	–75.2116	38.1585	1.3	0.98	1.2
	CB1029	–75.2142	38.2395	1.7	0.48	6.0
	CB1030	–75.1379	38.2592	1.9	0.97	1.2
	XDM4486	–75.1780	38.4132	0.9	0.96	3.3
	XDN6921	–75.1046	38.4284	1.4	0.94	3.2
	NPC0012	–75.2104	38.2414	1.6	0.67	5.4
	XBM8828	–75.2850	38.1483	1.4	0.96	1.8
	NOAA8570283	–75.0917	38.3283	4.4	0.97	2.1
Salinity					*RB*	*RMSD* (PSU)
	CB1018	–75.3683	37.8670	3.0	0.01	1.5
	CB1019	–75.3961	37.9813	2.3	–0.14	4.6
	CB1023	–75.2831	38.0914	1.9	–0.13	4.0
	CB1027	–75.2380	38.1493	2.2	–0.15	5.0
	CB1028	–75.2116	38.1585	1.3	–0.18	5.6
	CB1029	–75.2142	38.2395	1.7	–0.15	5.2
	CB1030	–75.1379	38.2592	1.9	0.03	3.2
	XDM4486	–75.1780	38.4132	0.9	0.42	9.5
	XDN6921	–75.1046	38.4284	1.4	0.49	11.6
	NPC0012	–75.2104	38.2414	1.6	–0.42	10.6
	XBM8828	–75.2850	38.1483	1.4	–0.23	7.3

the well-known Eulerian and Lagrangian means (Zimmerman, 1979; Cheng and Casulli, 1982), although for the purposes of this study we are not concerned with this decomposition but instead focus on how ⟨Q⟩ is affected by different physical processes. The time-averaged flux is evaluated during three periods in year 2014, namely March to May, June to August, and September to November, representing spring, summer, and fall seasons, respectively.

The time-averaged volume flux is decomposed into its different components with

$$\langle Q \rangle = Q_{wind} + Q_{tide} + Q_{river} + Q_{density} + Q_{wave}, \quad (2)$$

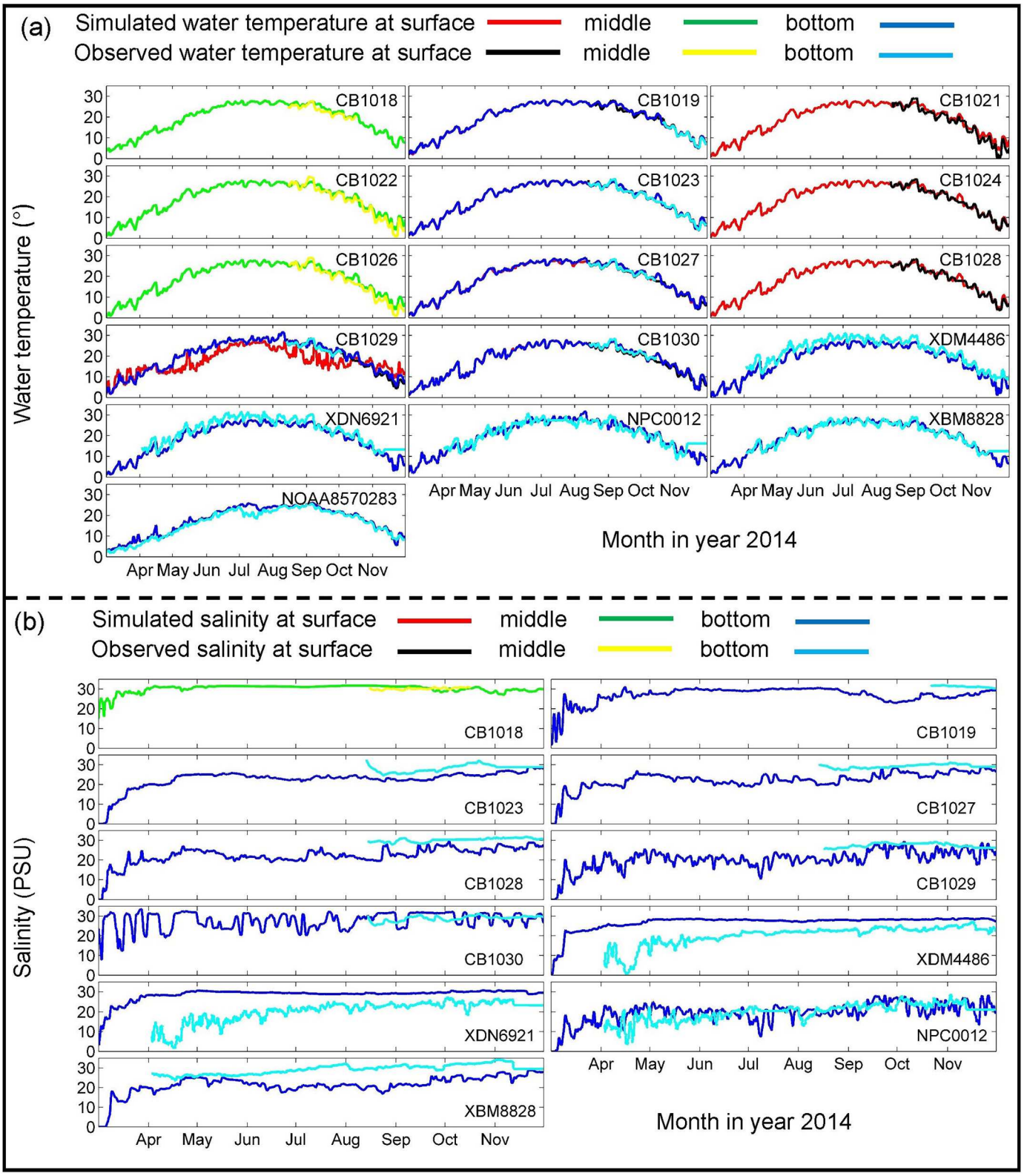

Fig. 2. Time series of (a) water temperature and (b) salinities from simulations versus observations during March–November 2014.

where Q_{wind}, Q_{tide}, Q_{river}, $Q_{density}$, Q_{wave} denote the volume flux contributed from winds, tides, river discharges, and baroclinically and wave-driven flows, respectively. The individual volume fluxes are calculated by the difference between the standardized model (e.g., including all physical processes) and that in the absence of one process. For example, the wind-driven flow Q_{wind} is calculated from the residual of the wave-current coupled model with and without including the wind forcing. The method of the quantitative analysis like this follows similarly for Q_{wave}, Q_{tide}, Q_{river}, and $Q_{density}$. It should be noted that both the wave-driven flux Q_{wave} and the tidally driven flux Q_{tide} could, in principle, be decomposed into their Eulerian mean and Lagrangian drift components. For the purpose of this paper, this decomposition process for the calculation of the total time-averaged flux was not further explored.

For the winds, it is well known that wind-driven circulation depends strongly on the geometry and that this effect is highly nonlocal. The typical wind-driven circulation in a channelized estuary is downwind in the shallow waters and upwind in the deep channel, thus revealing the possibility of wind-driven currents being in a direction that opposes the winds. To properly characterize these complex processes and to reliably assess the impact of other processes (e.g., surface gravity waves) on the volume fluxes, high-resolution and unstructured grid-based mesh (e.g., grid size being as small as 10 m) is applied in the shallow water regions and deep tidal channels.

2.4. Skill metrics

Model performance was evaluated using the Pearson correlation coefficient (*CC*), root-mean-square deviation (*RMSD*), mean bias (*MB*), and relative bias (*RB*), which were written as:

$$CC = \frac{\frac{1}{N}\sum_{n=1}^{N}(Mod_n - \overline{Mod})(Obs_n - \overline{Obs})}{\sigma_{Mod_n}\sigma_{Obs_n}}, \tag{3}$$

$$RMSD = \left[\frac{1}{N}\sum_{n=1}^{N}(Mod_n - Obs_n)^2\right]^{1/2}, \tag{4}$$

$$MB = \frac{1}{N}\sum_{n=1}^{N}(Mod_n - Obs_n), \tag{5}$$

$$RB = \frac{\sum_{n=1}^{N}(Mod_n - Obs_n)}{\sum_{n=1}^{N}|Obs_n|}, \tag{6}$$

where $\overline{Model}$ and $\overline{Obs}$ denote means of the modeled Mod_n and observed values Obs_n in a sample of size N; σ_{Mod_n} and σ_{Obs_n} are the corresponding standard deviations. Scores of *CC, MB, RB*, and *RMSD* reflect the linear correlation, mean and relative differences, and direct comparison between simulations and observations, respectively.

3. Results

3.1. Model skill assessment

Fig. 2 shows the time series of simulated water temperature and salinities versus observations from March to November 2014. Observed water temperature presented appreciable seasonal variations from spring to fall (e.g., 12, 25, and 18 °C), while their spatial variability was relatively weak. By contrast, observed salinities showed substantial spatial variations across the observed stations (e.g., low salinities near the creek while high values in CB). The wide spatial and long temporal features of hydrodynamics were well captured by the model, with ensemble *CC* and *RMSD* for water temperature being 0.92 and 2.2 °C, respectively (Table 1). Model-to-data bias for water temperature at CB1029 was partially caused by the lack of daily discharge at Newport River in 2014 (e.g., there is no Newport River, Ayres Creek flows into Newport Bay), which was estimated from the averaged values in the years 2001–2008 herein. As the influenced area by the river input is limited to nearby regions, this treatment is considered acceptable. Weak variability of the water temperature across all stations from surface to bottom layers indicated that the shallow lagoon was well mixed most of the time, in agreement with the previous study of *Kang and Xia* (2022). Given that stream discharges were ignored partly in the upper bays, the model showed a better skill for the salinity simulation in the lower bays (Table 1). For example, the *RB* and *RMSD* in the lower bays were in the ranges of –0.18 to 0.03 and less than 5.6 PSU, while they were from –0.42 to 0.49 and no less than 7.3 PSU in the upper bays. Dillow and Greene (1999) reported that the low freshwater discharges into the MCBs only affected salinities within nearby regions. After the successful assessment of the model skill, numerical simulations conducted over this lagoonal system will be presented and analyzed in the following subsections.

3.2. Seasonal circulation and exchange flows

Fig. 3 depicts spatial distributions of the seasonal circulation in the surface and bottom layers. Surface circulation (e.g., 0.05–0.15 m/s) was stronger than the bottom one (e.g., < 0.02 m/s), especially at tidal channels, within the deep inlets, and in the coastal ocean. Lagoonal circulation in the narrow SB was higher than that of AB and CB, presumably resulting from the complex wind–current–wave–bathymetry interaction in this narrowing backbay (Mao and Xia, 2018). Because of the limited exchange flows via tidal inlets, water currents in the lagoon were generally weaker than those in the coastal ocean. Occasionally, seasonal currents in the lagoon near OCI (e.g., in the upper SB and lower IWB) reached 0.25 (0.15) m/s in the surface (bottom) layer. In the lower IWB, a clockwise circular movement at a length scale of 1 km persisted across all three seasons (e.g., 0.2–0.3/0.1–0.2 m/s in the surface/bottom layer). Along AI and WI, the flow pattern was dominated by the northward currents. With respect to flow intensities, inlet circulation was ebb-dominated (e.g., up to 0.3 m/s jet flow at the mouth of OCI). Overall, the seasonal variability of the inlet dynamics and coastal circulation was relatively weak. Although water currents in the lagoon far away from the adjacent inlet were weak (e.g., < 0.05 m/s), they showed substantial variations from spring to fall (e.g., various flow directions).

Fig. 4 shows the net and absolute volume fluxes $<Q>$ from spring to fall across various transects of the MCBs. The greatest absolute $\langle Q \rangle$ occurred via CI–CB at 2137 m^3/s, which decreased as the distance from the nearby inlet increased (e.g., 403 and 656 m^3/s for IWB–AB and OCI–IWB). The absolute $\langle Q \rangle$ from SB to OCI (CB) was 394 (264) m^3/s. Overall, the exchange flows collectively depend upon the inlet width and its connectivity to the backbays. Net flows from OCI and CI to the coastal ocean were 36 and –129 m^3/s, respectively (i.e., in the directions of eastward and southward), confirming the ebb-dominated nature of the seasonal circulation.

While the net $\langle Q \rangle$ across the CB–NB was close to zero, it showed vertical inhomogeneity, e.g., two-layer estuarine circulation (e.g., 19/–40 m^3/s inflow/outflow in the bottom/surface layer in fall, see Fig. 4a). The weakness of seasonal circulation in AB and circular movement in IWB were well reflected by the low net $\langle Q \rangle$ across IWB (e.g., < 8 m^3/s). Despite the shallowness, the two-way flows appeared via OCI–IWB, CB–NB, CB–SB, and IWB–AB. Even for the one-way transport between the lagoon and coastal ocean via tidal inlets, magnitudes of the $<Q>$ varied significantly from surface to bottom layers (e.g., –45, –22, and –4 m^3/s in spring for CI). From spring to fall, the net $\langle Q \rangle$ showed directional variations between SB and OCI or CB. To further investigate the dynamics of seasonal circulation and exchange flows in the MCBs, the relative effects of local winds, tides, baroclinicity, and surface waves were discussed in the following section.

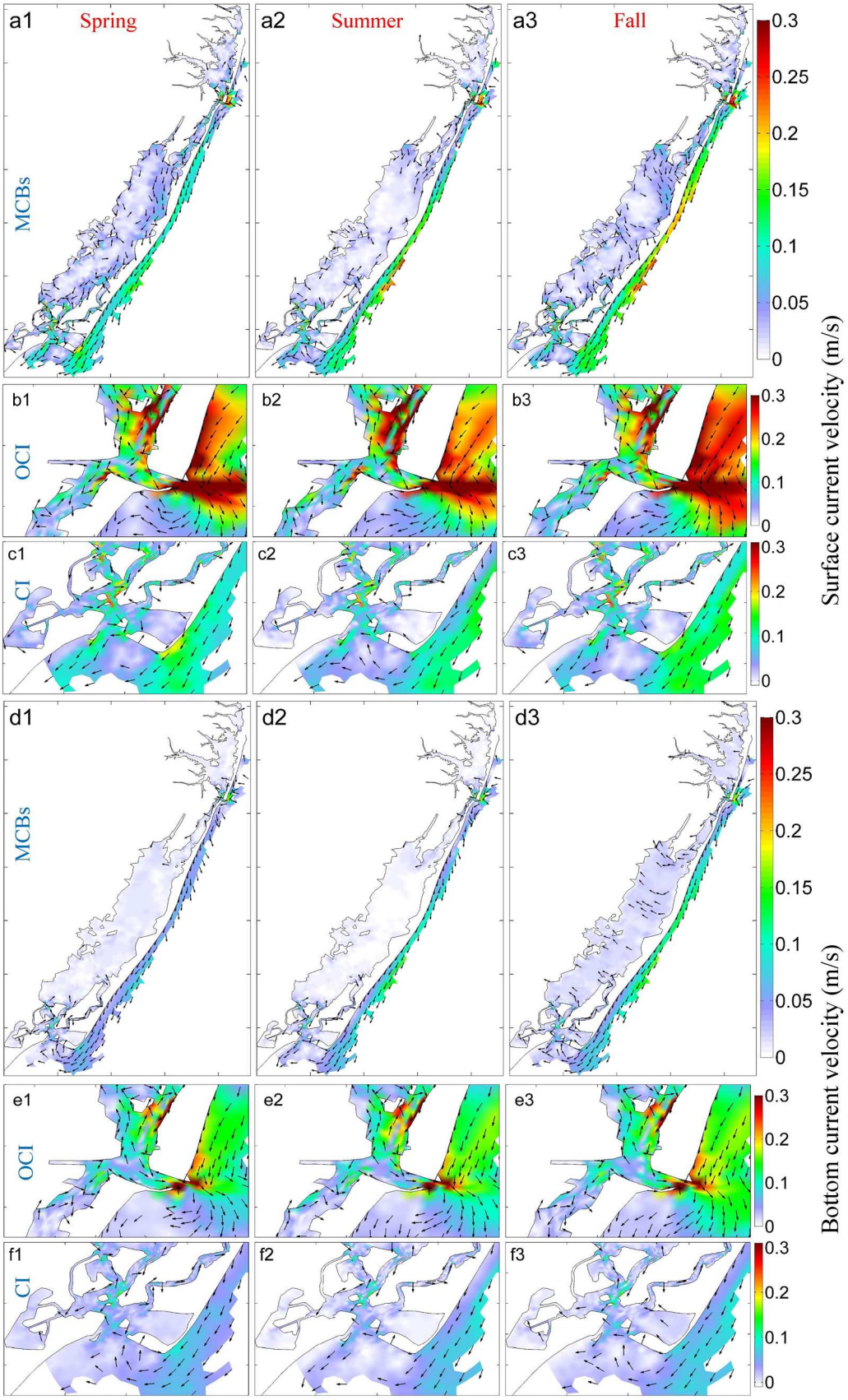

Fig. 3. Spatial distributions of the seasonal current velocities at the (a1–3, b1–3, and c1–3) surface and (d1–3, e1–3, and f1–3) bottom layers from the 3D wave–current coupled model in 2014. For clarity, arrows with velocities less than 2 cm/s are not shown in Figs. 3, 6, 8–11, and 13.

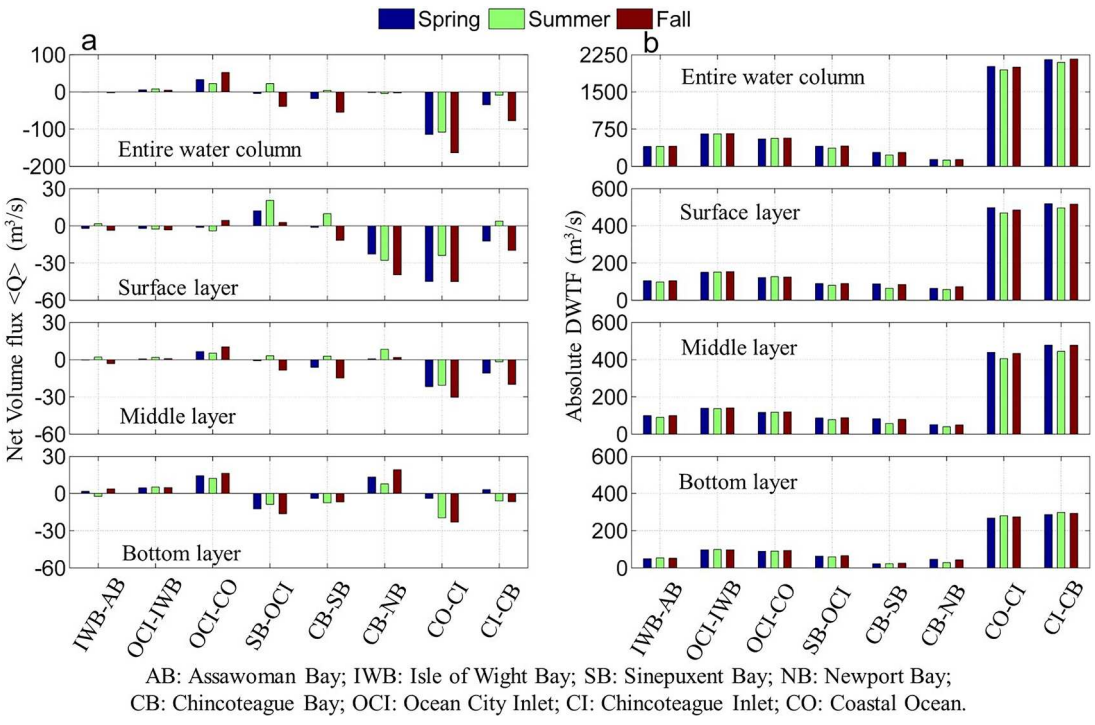

Fig. 4. Seasonal (a) net and (b) absolute ⟨Q⟩ from the 3D wave–current coupled model in 2014.

4. Discussion

4.1. Effect of local winds on seasonal dynamics

Considering the importance of winds to seasonal dynamics of the MCBs (Kang et al., 2017), the quality of the NARR data near the paired inlets (Figs. 1c–d) was examined against observations (Figs. 5a–b). The arithmetic means of the time series of the wind vector and the magnitude of the wind speed in spring, summer, and fall are defined as the vector-averaged wind and scale-averaged wind magnitude, respectively. Seasonal winds in spring and fall were stronger than those in summer. Although no preferential wind directions across three seasons were presented, stronger winds in spring and fall were mainly northwesterly (NW) while they are southerly in summer (Figs. 5c–e). The scale-averaged value of the observed wind was ~5 m/s in both spring and fall, whereas the vector-averaged one in the latter season was twice that of the former (e.g., 1.4 versus 0.7 m/s) due to the lower variability of the time series of the wind direction. It seems that the NARR model overestimated the scale-averaged wind magnitude during the fall season (e.g., 4.80 versus 4.55 m/s near OCI, and 4.97 versus 3.89 m/s near CI, see Fig. 5b). Studies conducted in the Gulf of Mexico have revealed that reanalysis wind tends to underestimate coastal wind patterns (Hsu et al., 2022). Consequently, this overestimation/underestimation can result in stronger/weaker simulation circulation in estuaries/coastal oceans. Given that the paired observations near the northern and southern inlets of the MCBs are not very consistent with each other (e.g., the directions of spring winds derived from NCEI and NDBC buoys are different, see Fig. 5a), the reanalyzed NARR winds that generally captured the wind pattern was adopted herein to avoid the uncertainties from the observed winds (e.g., only two buoys available currently). In Lake Michigan, the observation-based winds obtained using the Natural Neighboring Method with multiple buoys scattered both along the periphery and in the middle of the lake (Schwab and Morton, 1984; Lang and Leshkevich, 2014) have been successfully applied to simulate the water circulation and particle trajectories reasonably by Mao and Xia (2020a, b). Therefore, in the future, deploying additional wind buoys for comprehensive coverage across the entire MCBs (e.g., in the coastal ocean, within the inlets, and in the lagoon) could warrant consideration for using observed wind data to drive the model, as was previously done in the case of Lake Michigan.

Although wind fields were spatially uniform over the small domain of the MCBs (not shown herein), wind-induced circulation varied significantly among lagoon, inlets, and the coastal ocean (Fig. 6), presumably due to complex wind–bathymetry–geometry interactions (Salles et al., 2015; Kang et al., 2017). Lagoonal circulation driven by winds was stronger in the surface than that near the bottom (e.g., up to 0.15 versus < 0.02 m/s). Spatially, wind-driven surface circulation was more appreciable in the coastal ocean than that in the backbays away from the adjacent inlet. Seasonally, wind-driven surface currents over SB in spring and fall were much stronger than those in summer (e.g., 0.05–0.15 versus < 0.05 m/s), when the southwesterly currents were impeded by the confronting coastline extending inside from OCI. Wind-induced currents in spring were relatively strong, attributed to the better alignment between the major axis of SB and the local wind direction (Fig. 5a). Restricted by the shortness of the wind fetch over the relatively smaller area of the OCI, wind-induced inlet currents were relatively weak (e.g., below 0.05/0.02 m/s in the surface/bottom layer). The finding that the intensity of wind-induced flows is highly dependent on its coherence with the local geometry is consistent with previous studies in similar systems including the western Dutch Wadden Sea (Duran-Matute et al., 2016) and Curonian Lagoon (Umgiesser et al., 2016). Wind-induced bottom circulation in the coastal ocean resembled the surface one but with a reduced magnitude. By contrast, the surface and bottom circulation driven by winds in CB was distinct both in magnitude and direction (e.g., surface current was consistent better with local winds). Winds over the southern tip of AI in fall were large (Fig. 5a), resulting in stronger surface currents than those in spring (e.g., 0.15 versus 0.075 m/s).

Fig. 7a showed that the NW winds in spring and fall exported net $<Q>$ via OCI (15 and 4 m^3/s) and CI (–26 and –15 m^3/s), while southerly winds in summer imported –11 and 14 m^3/s. The relationship between wind direction and exchange flows across CI is consistent with the numerical study using constant winds from Kang et al. (2017), while it is different across OCI. Given that the small and narrow OCI is more

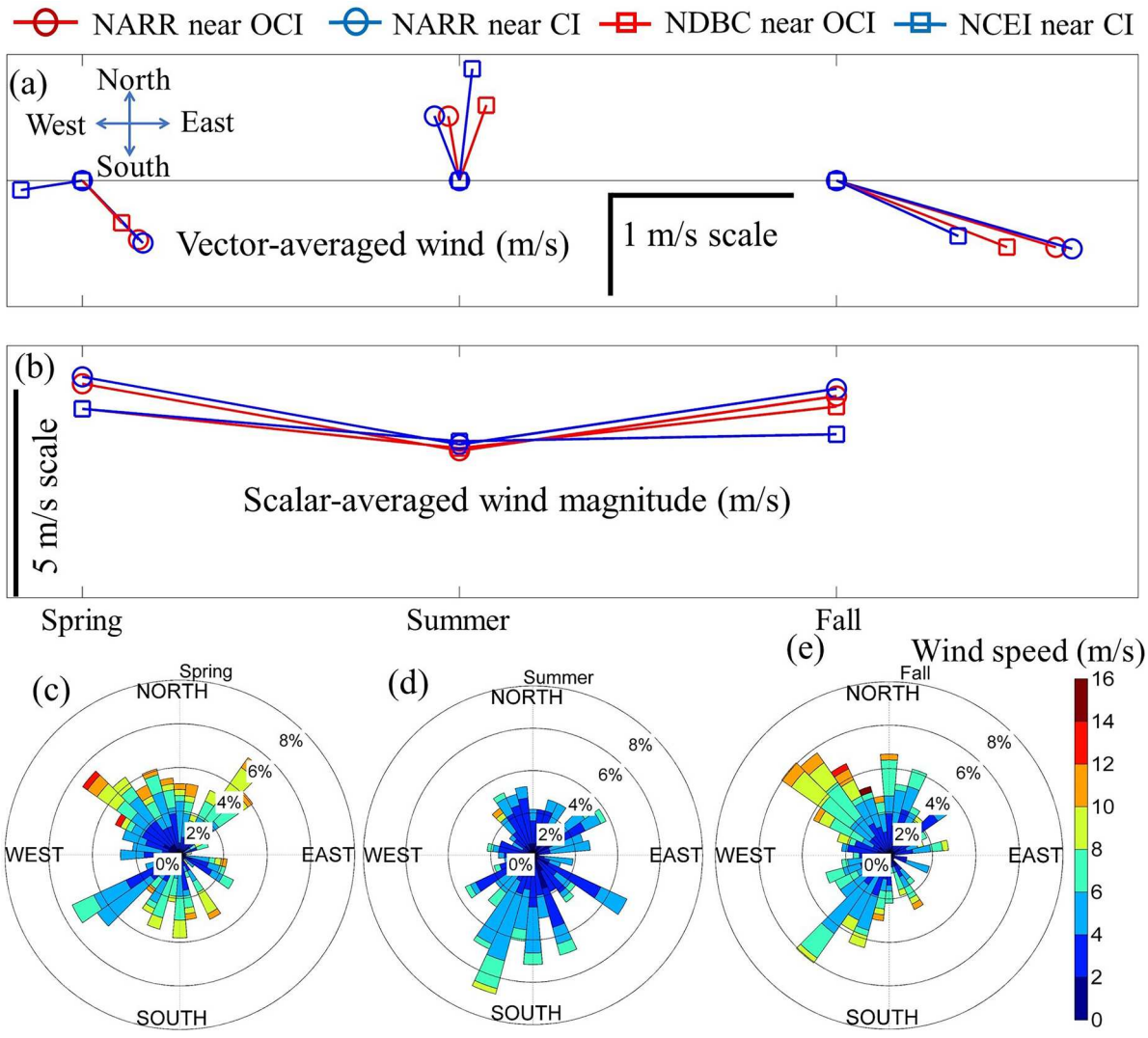

Fig. 5. Modeled and observed (a) vector- and (b) scalar-averaged seasonal winds near the OCI and CI; (c)–(e) wind roses from the NARR products over the MCBs in 2014. Note that the magnitude of the scale-averaged wind is the vertical distance from the red/blue circle/square signs to the horizontal.

sensitive to the temporal variations in local winds, the seasonally averaged transports in response to realistic winds could be more complex and variable. However, both studies support the conclusion that the directional alignment between winds and the inlet orientation are substantial to the direction and magnitude of the exchange flows between lagoon and the coastal ocean. Wind-induced net ⟨Q⟩ in the lower bays via SB (e.g., up to –33 m^3/s) was larger than that across IWB. In spring, wind-induced net ⟨Q⟩ via IWB–AB changed from surface to bottom layers (e.g., 12, –6 and –3 m^3/s). Between the lagoon and coastal ocean, vertical variations in wind-induced exchange flows via OCI were relatively weaker than that via CI, which showed surface/middle outflow and bottom inflow in spring. Therefore, the seasonally varying winds are critical to the water circulation and exchange flows in the shallow lagoon-inlet-coastal ocean system.

4.2. *Effect of tides on seasonal dynamics*

Fig. 8 shows the spatial distributions of tidally driven currents from spring to fall, which indicated that tides were the major factor contributing to the circulation of the MCBs (cf. Fig. 3). Near the bottom, tidally driven currents were quite weak in AB, northern IWB, and the shallow part of CB (e.g., less than 0.02 m/s). Compared to wind effects, tidally driven flows were much stronger in the coastal ocean, near inlets (e.g., above 0.3 m/s at the mouth of OCI), southern IWB, northern SB, and the tidal channels behind CI. This finding indicates that the relative effect of tides versus winds on the water circulation is mainly dependent upon the degree of exposure to the oceanic tides. Recent surface drifter observations indicate that the relative effects of winds on surface currents become stronger gradually in the regions moving further away from the adjacent inlets with tides becoming weaker (Fitzenreiter et al., 2022). Along the SB's principal axis, tide-induced surface flows reached 0.1–0.15 (0.05–0.1) m/s in spring (summer and fall), reducing to half in the bottom layer. Tidal currents via both inlets were mostly dominated by outflows at a seasonal timescale, while surface inflows occurred occasionally via CI in spring (cf. Fig. 7b). The phenomenon that the simulated water circulation and exchange flows between the paired inlets are different indicates that the unique inlet geometry can modulate tidal currents, e.g., in the Indian River Lagoon, Florida (Smith, 2001). A clockwise circular tidal flow at a length scale of about 1 km diameter formed in the southern IWB across all three seasons and layers. This closed water circulation likely retains nutrients, reduces lagoonal exchanges, increases residence time (cf. Umgiesser et al. (2014) for similar lagoonal systems in the Mediterranean Sea), which could further result in poor water quality in upper bays (IAN, 2015).

Overall, tides generated a larger amount of net ⟨Q⟩ than winds (Figs. 7a–b). Across the CO–CI (note: CO is the abbreviation for coastal

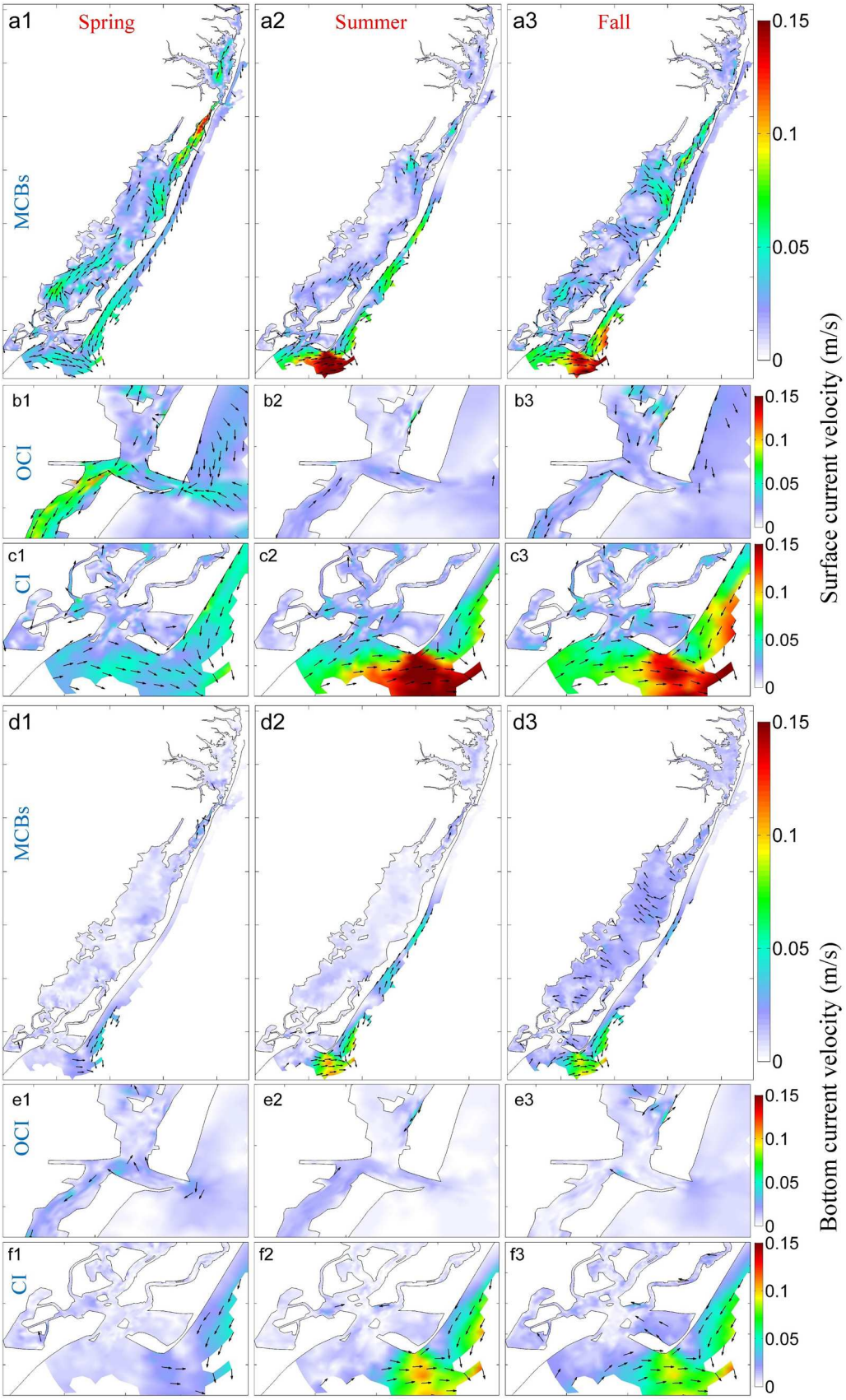

Fig. 6. Spatial differences of seasonal current velocities produced from the model with and without local winds in 2014 at the surface (a1–a3, b1–b3, and c1–c3) and (d1–d3, e1–e3, and f1–f3) bottom layers.

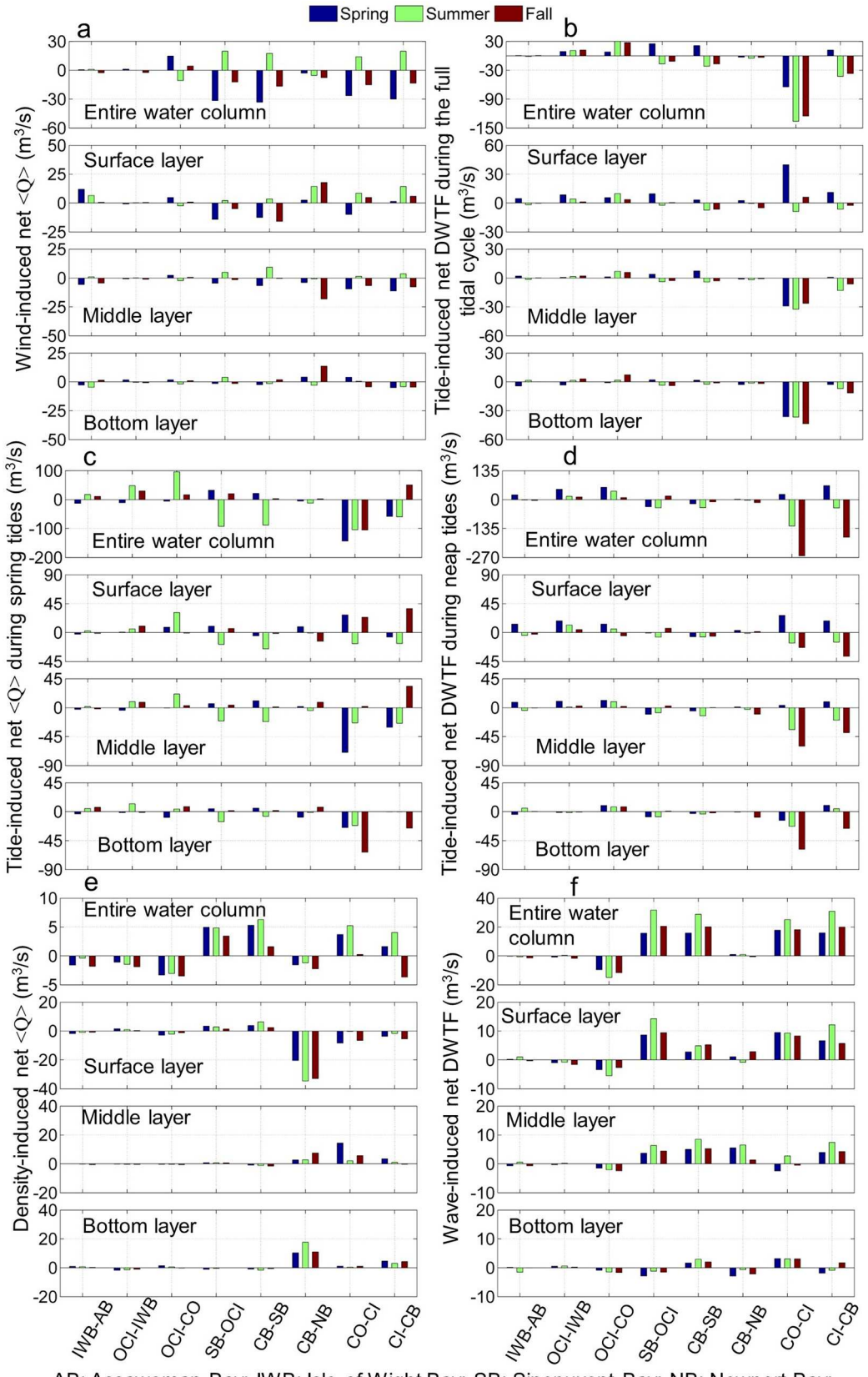

Fig. 7. Seasonal net ⟨Q⟩ induced by (a) winds, (b) tides, (c) spring and (d) neap tides, (c) density, and (d) waves in 2014.

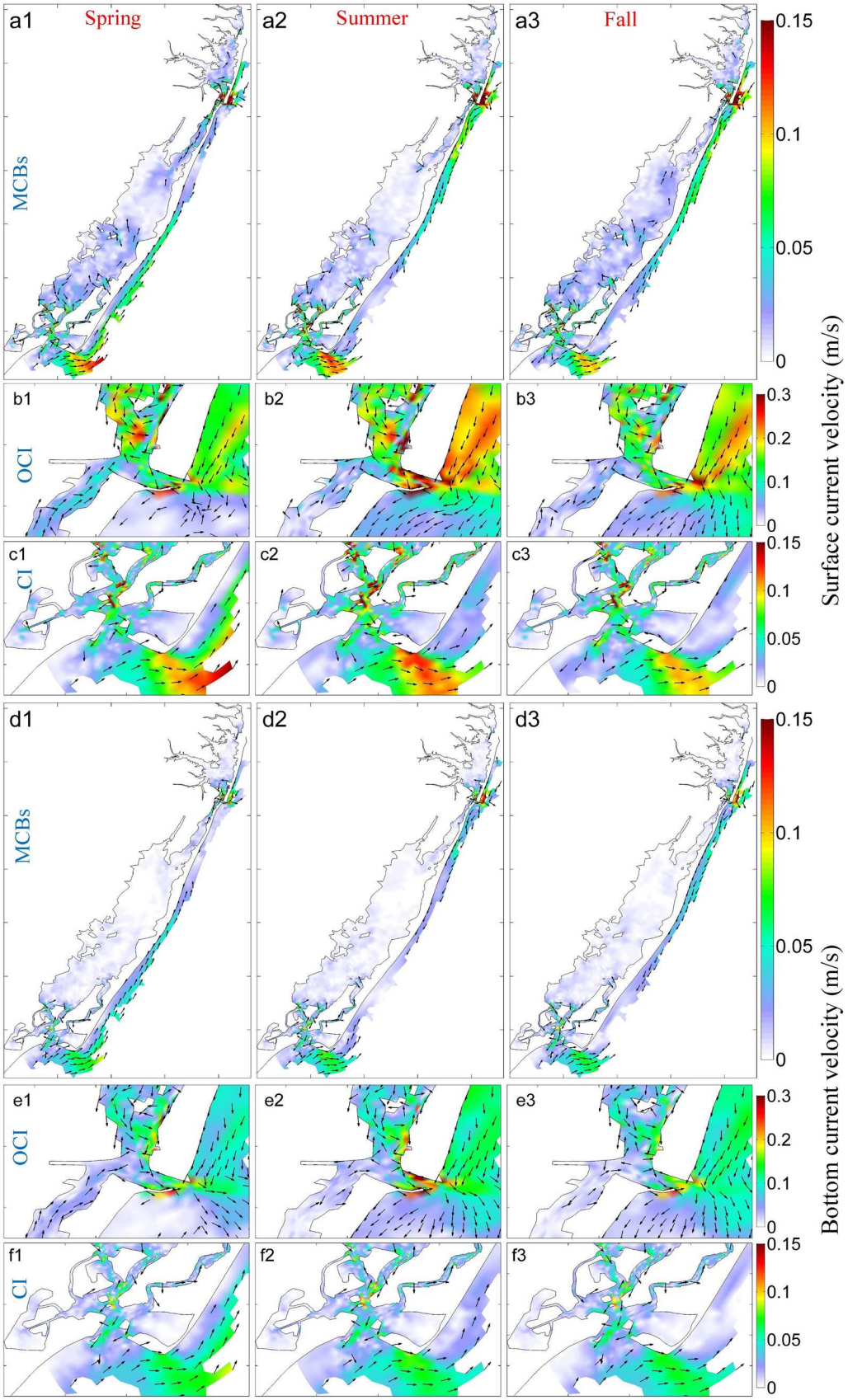

Fig. 8. Spatial differences of seasonal current velocities produced from the model with and without tides in 2014 at the surface (a1–a3, b1–b3, and c1–c3) and (d1–d3, e1–e3, and f1–f3) bottom layers.

ocean), tide-induced net ⟨Q⟩ reached –136 m^3/s. By contrast, the volume flux across the small OCI was below 31 m^3/s. From spring to fall, volume fluxes in the surface layer were 40, –9, and 6 m^3/s, and they were –29, –32, and –26 (–36, –37, and –43) m^3/s in the middle (bottom) layer. As a result of the local modulation by the narrow and deep tidal channels, tide-induced net ⟨Q⟩ from CI to CO differed significantly from that to CB (e.g., –64, –136, and –125 versus 12, –43, and –37 m^3/s during spring, summer, and fall, respectively). Overall, tide-induced exchange flows between the adjacent backbays were weak, except for SB–OCI, CB–SB, and CI–CB in spring (e.g., 25, 21, and 12 m^3/s). Valle-Levinson et al. (2018) reported that inlet exchanges in the Wadden Sea are different between the spring and neap tides. For the sites near the paired inlets of the MCBs, tide-induced currents showed similar patterns between both tidal cycles (e.g., the presence of intense inlet flows and circular movements in IWB, see Figs. 9 and 10). In SB and the coastal ocean, the circulation driven by the spring tide was stronger than that by the neap one. The net ⟨Q⟩ from CI to CO was negative overall, except for that in the spring season at the neap tide (e.g., –143 (25), –104 (–123), and –105 (–263) m^3/s at the spring (neap) tide in the seasons of spring, summer, and fall). The largest number of exchange flows in fall at the neap tide was well reflected by the spatial distributions of the seasonal circulation (e.g., consistent outflows shown in Figs. 10c3 and f3). Therefore, tides play a substantial role in the seasonal and spatial variations in the water circulation and exchange flows, especially near the inlet and along the coastal ocean.

4.3. Effect of density variations on seasonal dynamics

Fig. 11 shows the contribution of density gradients to the seasonal circulation, which was relatively weaker (e.g., < 6 cm/s) compared with that from tides or winds, consistent with the findings in the western Dutch Wadden Sea (Buijsman and Ridderinkhof, 2007). Seasonal variability of the density-induced net $<Q>$ was weak as well, except for that via CI–CB (e.g., northward in spring and summer, while southward in fall). As a result of freshwater discharge of the nearby Ayers Creek, density-driven flows in NB reached 6 (2) cm/s in the surface (bottom) layer. Via the section between NB and CB, seasonal circulation was represented by surface outflows (e.g., –29 m^3/s) and middle/bottom reversals (e.g., 4/13 m^3/s, meaning the flow is reversed from surface to middle and bottom). Between CI and CO, exchanging features were indicated by surface outflows and middle/bottom inflows (e.g., –5 and 7/1 m^3/s). In the well-mixed shallow inlets, tracers are usually homogeneous in the vertical direction of the water column. However, during the passage of hurricanes or strong wind events (e.g., bringing strong precipitation and high peak river flow from creeks), water salinities and larval density are vertically inhomogeneous at the stratified tidal inlets (Kang and Xia, 2022). Under these conditions, consideration of the density-induced, two-way flows in the 3D hydrodynamic model could help estimate salt flux and larval recruitment better in the lagoonal system.

Fig. 12 shows spatial distributions of water temperature, salinities, and densities, suggesting that density gradients are primarily caused by the spatial variations in salinities (e.g., similar patterns in space). Based on the linearized Equation of State [$\rho = 1000 - 0.15(T - 10) + 0.78(S - 35)$], density ρ is determined collectively by the water temperature T and salinity S. Spatial variations in water temperature were less than 2 °C in the MCBs while they reached 30 PSU for salinity. Consequently, the density changes due to water temperature were much smaller than that due to salinity (e.g., 0.3 versus 23.4 kg/m^3). This result is consistent with the statement from Mohanty and Panda (2009) for the small Chilika Lagoon, India (e.g., surface areas in the range of 815–992 m^2). The greatest spatial variability of the salinity in NB led to the intense density-driven currents (cf. Fig. 11) and relatively large net ⟨Q⟩ via CB–NB (Fig. 7e). The lowest salinity was close to the mouth of Ayers Creek (note: location was shown in Fig. 1b), which increased gradually towards the adjacent inlet.

4.4. Effect of surface gravity waves on seasonal dynamics

Fig. 13 shows the wave-driven seasonal circulation, which was significant near the inlets and in the coastal ocean, especially for the surface layer. Ocean swells propagating from offshore regions started breaking as they approached shallower areas (Mao and Xia, 2018), subsequently generating intense longshore currents with magnitudes up to 0.15 m/s. In addition to the MCBs (Mao and Xia, 2018), similar phenomena were reported previously in the Willapa Bay, WA (Olabarrieta et al., 2011) and the New River Inlet, NC (Chen et al., 2015). In the shallow lagoon-inlet-coastal ocean system, the seasonally averaged wave-driven currents (e.g., up to 30 cm/s) were relatively larger than those in the nearshore of Lakes Erie (e.g., < 4 cm/s) (Niu and Xia, 2017) and Michigan (e.g., < 2 cm/s) (Mao and Xia, 2020a). Given that local wind-induced waves were substantially dissipated by the bottom friction and depth-induced breaking, wave-induced circulation was relatively weak (e.g., < 2.5 cm/s) in the shallow lagoon at water depths < 2 m, except for that in the lower IWB (e.g., reaching 30 cm/s) where the water depths were in the range of 5–10 m. Because coastal swells are higher than wind-waves in the MCBs (Mao and Xia, 2018), wave-induced currents in the coastal ocean were stronger than those in the lagoon. Overall, the relative contribution of waves to the seasonal dynamics of the MCBs was larger than that by density variations, but weaker than that caused by tides or winds. Wave-induced exchanges showed indiscernible variability of the magnitude for inflows across the three seasons via OCI and CI (e.g., –12 and 20 m^3/s). This phenomenon could be explained by the fact that breaking waves in the coastal ocean induce setup, which partially blocks the ebb flow and further leads to more inlet-directed mass flux and exchange flows in the onshore direction (Wargula et al., 2018). In the vertical space, wave-induced circulation, and net $<Q>$ varied significantly both in the shallow lagoon and deep inlets (e.g., 14 and –1 m^3/s in summer via SB–OCI). This inhomogeneity of seasonal dynamics from surface to bottom layers driven by waves is presumably caused by the vertical variations in 3D radiation stress gradients (Mellor, 2015), which generate relatively stronger currents near the surface layer (Mao and Xia, 2018).

4.5. Model limitations and future perspectives

The present study applied the three-dimensional, wave–current coupled hydrodynamic model to a shallow lagoonal system at a seasonal timescale. The validation experiments presented by Mao and Xia (2018) show that the model accurately predicts the dominant processes associated with the hurricane event at a timescale of several days (e.g., ~2 d starting from 16:00 8/27 to 18:00 8/28, 2011). With the inclusion of baroclinic processes (e.g., salinity and temperature induced density-driven currents), further validations have been conducted for water temperature and salinities in the surface, middle, and bottom layers herein (Fig. 2). To examine the model ability of predicting tidal-scale processes at a timescale of several months, simulated tidal levels and currents were compared with observations (e.g., for the period of 8/16–11/30, 2014 at a seasonal timescale) located near the inlets and in the lagoon (e.g., Table 2 for the calculated statistics and Fig. 1 for the location of observations). Although errors in estimating tidal levels and currents appear to average roughly 5 cm and 5 cm/s for the root-mean-square deviation (*RMSD*), the mean bias (*MB*) are less than 0.01 cm and 0.02 cm/s and the relative bias (*RB*) is less than 2 % (e.g., the error in predicting the seasonal mean of the current velocity vector is only 2 % of the observed results), which is acceptable for this study. When calculating the seasonally mean water circulation, the hourly current velocities produced from the model are the arithmetic mean, i.e., the time-averaged value is taken as the vector mean. Based on Table 2, the *MB* of the residual current is of O (0.02 cm/s). Assuming an inlet width of O (1 km) and depth of O (1 m), the error in calculating the flux is of O (0.2 m^3/s), which is negligible compared to the average volume flux arising from different processes and/or seasons of O (10

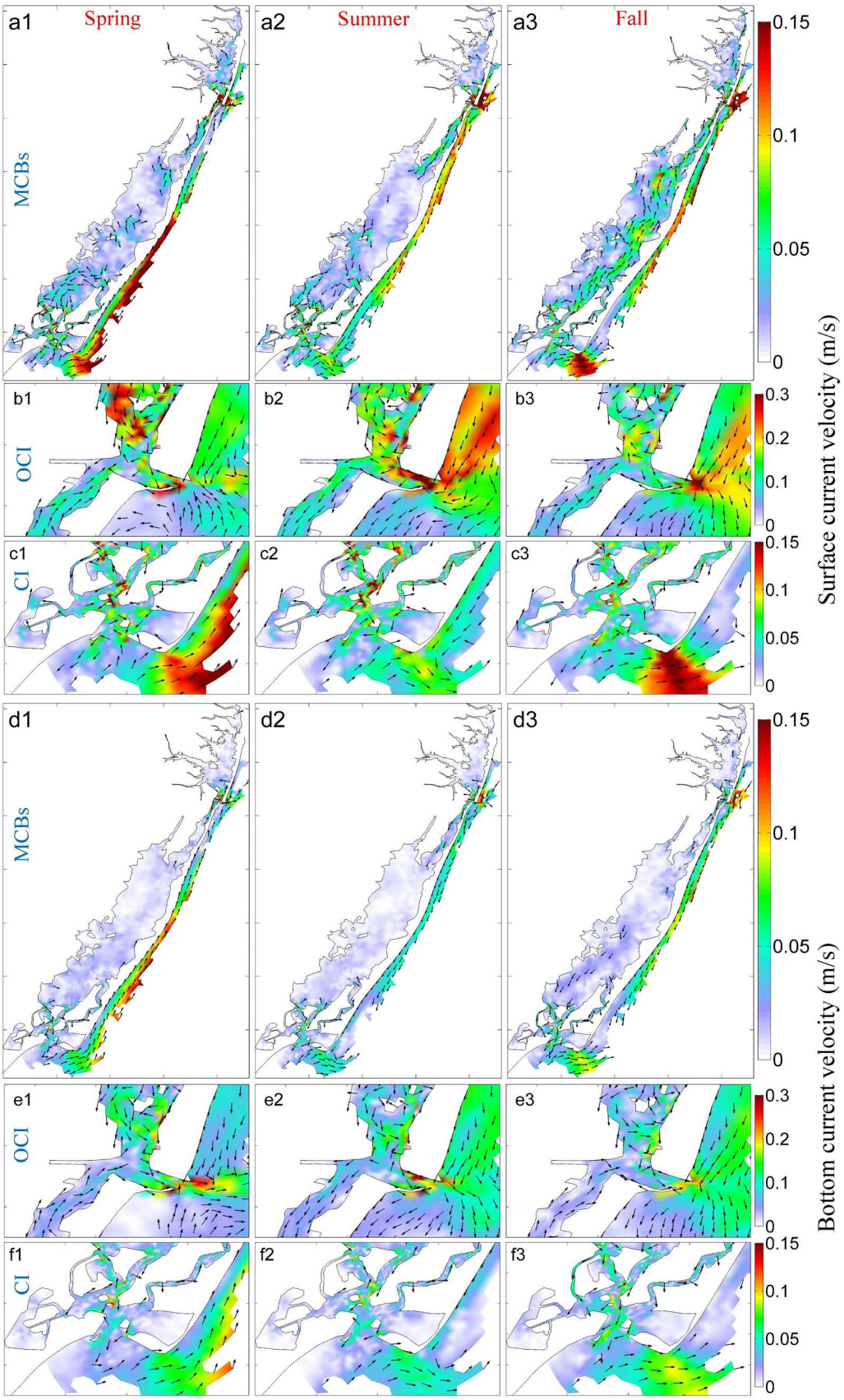

Fig. 9. Spatial differences of seasonal current velocities produced from the model with and without tides during the spring tide in 2014 at the surface (a1–a3, b1–b3, and c1–c3) and (d1–d3, e1–e3, and f1–f3) bottom layers.

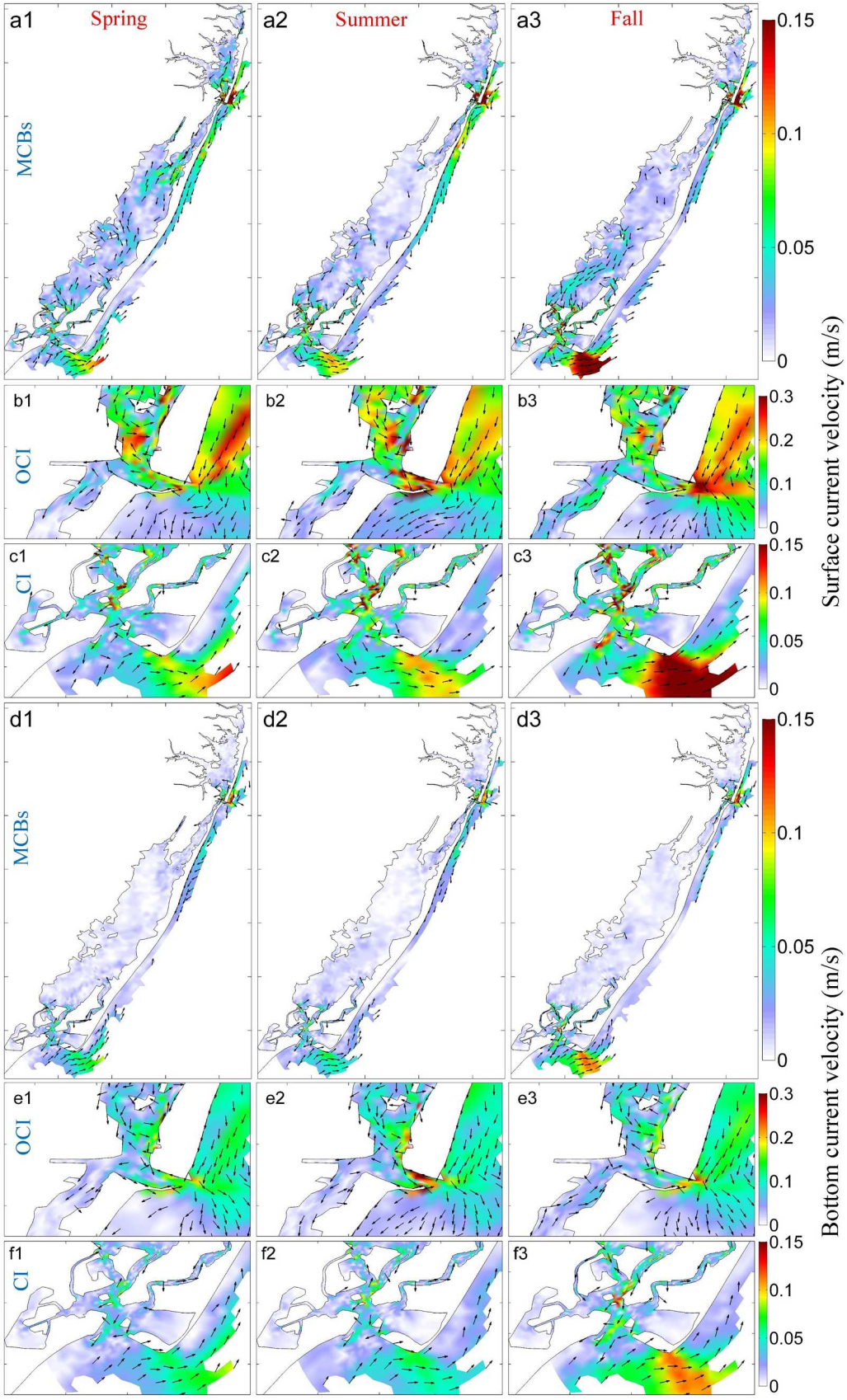

Fig. 10. Spatial differences of seasonal current velocities produced from the model with and without tides during the neap tide in 2014 at the surface (a1–a3, b1–b3, and c1–c3) and (d1–d3, e1–e3, and f1–f3) bottom layers.

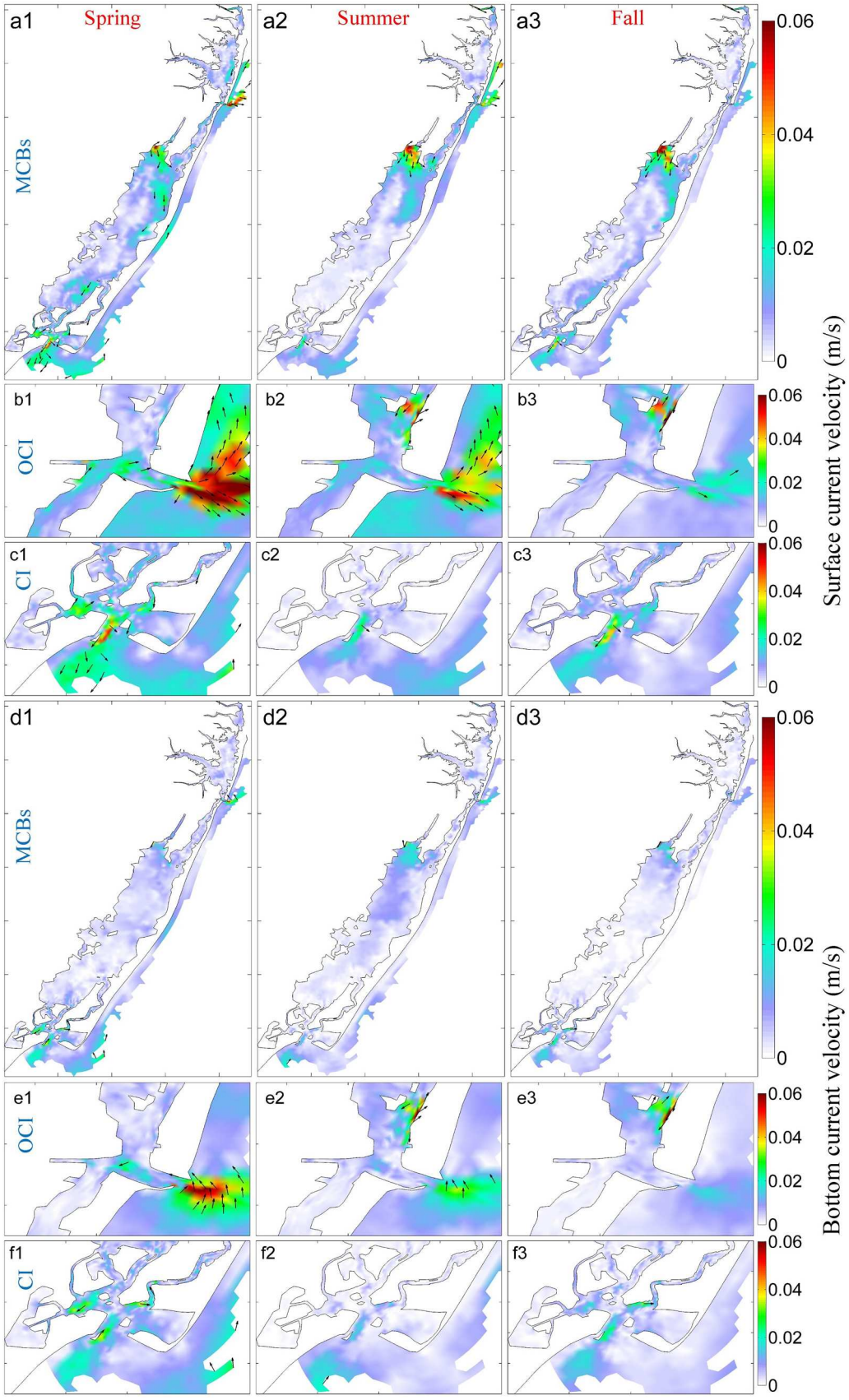

Fig. 11. Spatial differences of seasonal current velocities produced from the model with and without density variations in 2014 at the surface (a1–a3, b1–b3, and c1–c3) and (d1–d3, e1–e3, and f1–f3) bottom layers.

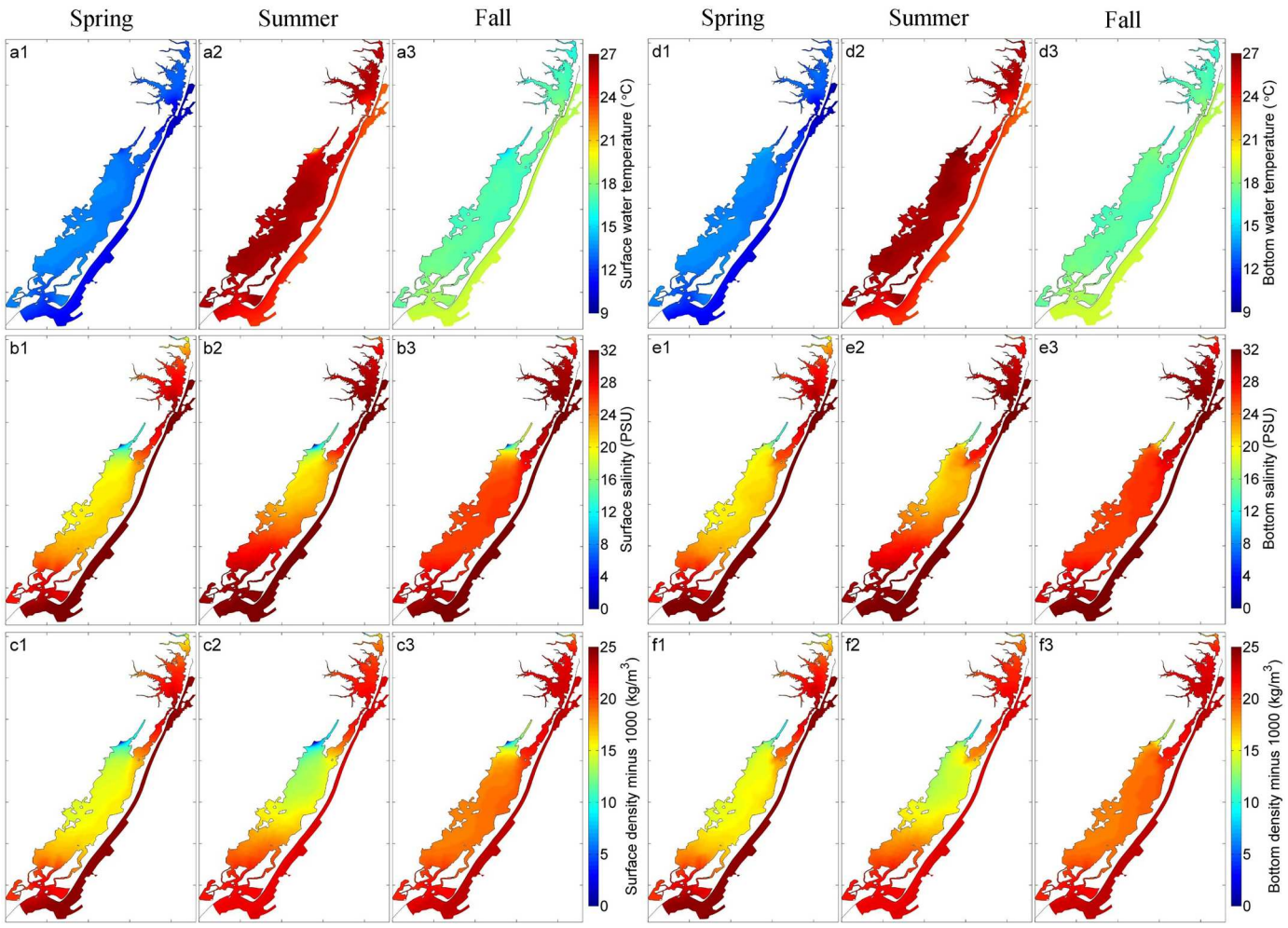

Fig. 12. Seasonal (a1–a3) surface water temperature, (b1–b3) salinities, and (c1–c3) sigma density (i.e., density minus 1000 kg/m^3) in 2014; (d1–d3), (e1–e3), and (f1–f3) are the same as (a1–a3), (b1–b3), and (c1–c3) except for that these variables are taken at the bottom layer.

m^3/s). To further investigate the model performance in simulating the tidal processes, the observed and simulated tidal amplitudes and phases for the major tidal components are compared in Table 3. The M2 tide is the dominant component in the domain over the MCBs. The major components of the observed tides showed a decreasing trend from the inlet into the lagoon (e.g., the M2 tidal amplitudes of 29 and 7.7 cm at stations NOAA and CB1028, respectively), which was reasonably captured by the model.

It should be noted that the predicted salinity appears to be off the observed one by 7–12 PSU at stations XDM4486, XDN6921, NPC0012, and XBM8828. Because the flow data near these stations is not available and thus not included in the model, the overestimation is attributed to the lack of freshwater discharges in calculating the nearby salinity. Given that the spatial influences of stream flows are limited near its mouth, the result is acceptable for this study that focuses on the general circulation over the entire shallow lagoonal system of the MCBs with limited river flow (Wang et al., 2013). With additional observations of freshwater discharges at these sites from the Maryland Department of Natural Resources, it would be a worthwhile future endeavor to estimate the salinity more accurately by considering the stream discharge from the adjacent watershed in the hydrodynamic model. A recent study indicates that the effect of salinity distributions near the river mouth are very localized, and the removal of inflows into the Hillsborough Bay will not significantly affect the mean estuarine circulation in the Tampa Bay (Chen et al., 2023).

Another possible source of the error in the salinity predictions overall is the use of just five sigma levels in the model, which may not be able to accurately resolve the delicate interplay between horizontal transport and vertical turbulent mixing of salinity. With less layers, the mixing is largely numerical and overpredicted, thus it gives an underprediction of the magnitude of the baroclinic circulation (Klingbeil et al., 2018). Given that the use of five sigma layers for the salinity calculation in the MCBs has been well validated under various weather conditions (e.g., weak, strong, and hurricane winds) (Kang et al., 2017; Kang and Xia, 2020; 2022), and that the computational cost for the unstructured-grid, wave-current coupled model is relatively expensive, this setting in the vertical coordinate is acceptable and thus adopted herein. It would be a worthwhile endeavor in the future to focus more quantitatively on individual processes based on numerical modeling (e.g., the effect of vertical resolution on the baroclinic flux) or specifically on the physics (e.g., investigations of plume dynamics near the river mouth during high and low discharge conditions). Besides, there is still room for further improvement in the coastal circulation modeling by parameterizing bottom frictional drags (e.g., bottom roughness, bedform, vegetation), wave breaking, and air-sea interactions in the wave-current coupled model, and by including additional modules of sediment transport and morpho dynamics in the integrated modeling system (Fringer et al., 2019).

Another limitation of this work is the method by which we extract each component with prerequisites, which assumes that different dynamic processes do not interact with each other. For example, the wind/tide effects are outlined by residual circulation and exchange flows be-

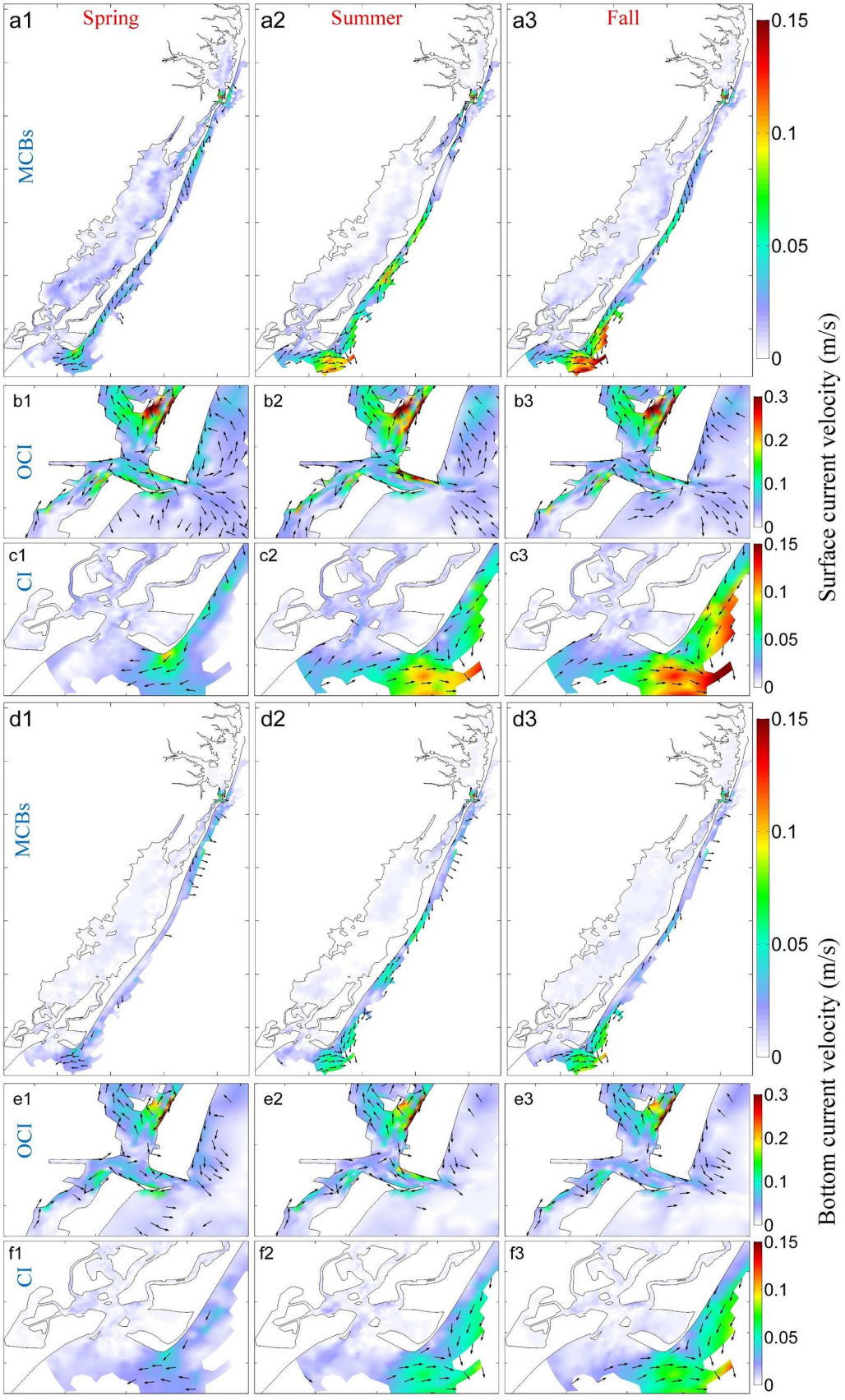

Fig. 13. Spatial differences of seasonal current velocities produced from the model with and without waves in 2014 at the surface (a1–a3, b1–b3, and c1–c3) and (d1–d3, e1–e3, and f1–f3) bottom layers.

Table 2
CC, RMSD, MB, and *RB* for the tidal levels and currents in the west–east and south–north directions, respectively. Statistics are calculated for the period of 8/16–11/30, 2014.

Variable	Station	*CC*	*RMSD*	*MB*	*RB*
Tidal levels	NOAA	0.96	8.9 cm	-5.3×10^{-5} cm	−0.02 %
	CB1019	0.90	3.9 cm	-3.5×10^{-5} cm	−0.05 %
	CB1028	0.98	2.2 cm	3.0×10^{-5} cm	0.06 %
Average of absolute value		0.95	5.0 cm	3.9×10^{-5} cm	0.04 %
Tidal currents in the west–east direction	CB1019	0.94	3.0 cm/s	0.5×10^{-3} cm/s	0.01 %
	CB1020	0.80	6.9 cm/s	7.0×10^{-3} cm/s	0.25 %
	CB1023	0.74	4.9 cm/s	5.0×10^{-3} cm/s	0.45 %
	CB1027	0.86	1.2 cm/s	0.6×10^{-3} cm/s	0.05 %
	CB1028	0.95	13.6 cm/s	16.6×10^{-3} cm/s	1.41 %
	CB1029	0.87	0.9 cm/s	-1.4×10^{-3} cm/s	−0.09 %
	CB1030	0.97	2.6 cm/s	4.0×10^{-3} cm/s	0.05 %
Average of absolute value		0.88	4.7 cm/s	5.0×10^{-3} cm/s	0.33 %
Tidal currents in the south–north direction	CB1019	0.96	4.5 cm/s	-3.6×10^{-3} cm/s	−0.03 %
	CB1020	0.88	8.4 cm/s	5.6×10^{-3} cm/s	0.07 %
	CB1023	0.98	4.9 cm/s	2.6×10^{-3} cm/s	0.02 %
	CB1027	0.95	2.0 cm/s	1.2×10^{-3} cm/s	0.03 %
	CB1028	0.90	8.7 cm/s	7.1×10^{-3} cm/s	0.46 %
	CB1029	0.92	1.5 cm/s	-0.3×10^{-3} cm/s	−0.01 %
	CB1030	0.97	3.5 cm/s	2.7×10^{-3} cm/s	0.02 %
Average of absolute value		0.94	4.8 cm/s	3.3×10^{-3} cm/s	0.09 %

Table 3
Observed and simulated tidal amplitudes and phases for the major tidal components during the period of 8/16–11/30, 2014.

	Tidal component	M2	N2	S2	O1	K1	Q1
Station		Tidal amplitudes (cm)					
NOAA	Observed	29	6.3	5.6	4.5	4.8	0.81
	Simulated	19	4.1	3.8	3.5	3.9	0.67
CB1019	Observed	11	2.4	2.2	2.2	2.1	0.67
	Simulated	7.9	1.7	1.5	2.1	1.8	0.36
CB1028	Observed	7.7	1.7	1.4	2.3	1.3	0.54
	Simulated	10	1.5	1.3	2.0	2.3	0.50
		Tidal phases (°)					
NOAA	Observed	10	344	22	199	209	166
	Simulated	24	359	34	224	234	188
CB1019	Observed	49	29	75	240	234	198
	Simulated	73	54	113	262	271	255
CB1028	Observed	132	113	146	288	303	295
	Simulated	139	119	163	283	288	235

tween the cases with and without including winds/tides. Supposing that only the winds/tides are included and running two cases to extract the wind-driven flows with $\langle Q \rangle_{all} = Q^{all}_{wind} + Q^{all}_{tide}$ and $\langle Q \rangle_{nowind} = Q^{nowind}_{tide}$, where the notation is used to imply that the components are not the same in each run due to nonlinear interactions between the processes. To illustrate this point, suppose we extract the wind-driven flux with $\langle Q \rangle_{wind} = \langle Q \rangle_{all} - \langle Q \rangle_{nowind} = Q^{all}_{wind} + (Q^{all}_{tide} - Q^{nowind}_{tide})$. The term in parentheses may be small but it is not necessarily zero. Considering a strong wind that could increase the water level and depth at the mouth, thus altering the tidally driven flux and rendering $Q^{all}_{tide} - Q^{nowind}_{tide} \neq 0$. Similarly, if we extract the tidally driven flux with $\langle Q \rangle_{tide} = \langle Q \rangle_{all} - \langle Q \rangle_{notide} = Q^{all}_{tide} + (Q^{all}_{wind} - Q^{notide}_{wind})$, the nonlinear term $Q^{all}_{wind} - Q^{notide}_{wind}$ could be nonzero. However, for the purposes of this study it suffices to assume the nonlinear interactions are weak enough such that our method provides a reasonable estimate of the relative impacts of the different processes on the flux.

5. Conclusions

This study successfully applied a three-dimensional, wave–current coupled Finite- Volume Community Ocean Model to a shallow lagoon-inlet-coastal ocean system, i.e., the Maryland Coastal Bays system (MCBs). The model-to-data comparison of hydrodynamic variables, including water temperature, salinities, tidal levels and currents at various vertical layers from spring to fall 2014, verified that the model skill was satisfactory at a seasonal timescale. The high-resolution and accurate model has successfully assessed various dynamic processes on the water circulation and exchange flows. Relative contributions of winds, tides, density variations, and waves to seasonal dynamics of the water circulation and exchange flows have been discussed in detail, and the main conclusions are summarized as follows:

1 Seasonal circulation in the surface is stronger than that near the bottom in the lagoon and near the inlets (e.g., 0.05–0.15 versus 0–0.02 m/s). Seasonal dynamics are primarily driven by tides, modulated by winds, waves, density variations, and regulated by the inlet orientation and geometry. Seasonal exchanges via the paired inlets are dominated by net outflows, which are primarily controlled by tides, and partially set off by the breaking wave-induced effects in the coastal region.
2 In spring and fall, northwesterly winds averaged at about 5 m/s led to southward water movements in the narrow Sinepuxent Bay and net outflows via the paired inlets. In summer, southerly winds averaged at about 3.5 m/s result in northward flows in Sinepuxent Bay and net inflows via both inlets. Wind-induced water circulation and exchange flows are regulated by the degree of the directional alignment between winds and local geometry (e.g., the positioning of the bay's principal axis and the inlet's orientation).
3 In Isle of Wight Bay, tidally driven currents are the primary contributors to the clockwise and circular movements, and the wave-induced circulation is important as well. Both tide and wave-induced currents are intense in the coastal ocean and near the inlet, but weaker in the shallow lagoon with the increasing distance moving away from the adjacent inlet (e.g., backbays are less affected by the ocean tides and remote swells propagating from the offshore regions).
4 Spatial variations in the salinity are responsible for the density-induced currents and exchange flows, especially at the mouth of Newport River in Newport Bay. Variations in density-induced circulation and exchange flows are weak across the three seasons, while they are relatively strong in spatial terms (e.g., from surface to bottom layers or from the river mouth to other regions of backbays) in this shallow lagoon-inlet-coastal ocean system.

The timescale of previous studies in the MCBs is mostly in the orders of several days (e.g., during episodic events), and the modeling results from this work could enhance our understanding of the coastal dynamics at a longer timescale (e.g., across seasons over several months). Effects of surface gravity waves on the dynamics of this system have been included and explored, and more effort and future work are expected to specify each of the individual wave effects (e.g., wave radiation stress, wave-induced surface roughness and bottom friction) on seasonal

dynamics both locally and remotely in this system. Furthermore, comparisons between seasonal and episodic dynamics of the lagoonal circulation and exchange flows in the MCBs need to be elucidated. This modeling method and its successful application to the MCBs would be useful for other similar lagoons and bays along the US East Coast (e.g., the Great South Bay in New York, the Barnegat Bay in New Jersey, the Indian River Lagoon and Tampa Bay in Florida, and the Perdido Bay in Alabama) and around the Mediterranean Sea in Europe (Umgiesser et al., 2014), which share similar characteristics for the study of the dynamic response to the combined effects of tides, winds, density variations, and waves across seasons.

CRediT authorship contribution statement

Miaohua Mao: Methodology, Software, Investigation, Validation, Visualization, Formal analysis, Investigation, Writing – original draft. **Meng Xia:** Conceptualization, Methodology, Software, Investigation, Resources, Writing – review & editing, Supervision, Project administration, Funding acquisition.

Declaration of Competing Interest

The authors declare that they have no known competing financial interests or personal relationships that could have appeared to influence the work reported in this paper.

Data availability

Data will be made available on request.

Acknowledgements

This research was partially supported by the National Science Foundation (NSF) No. 1856630 (PI: Dr. Xia). We would like to acknowledge high-performance computing support from the Cheyenne (doi:10.5065/D6RX99HX) provided by NCAR's Computational and Information Systems Laboratory (Project code: UMES0002), sponsored by the National Science Foundation. The authors greatly appreciate the Editor (Dr. O. Fringer) and anonymous reviewers for their constructive comments that significantly improve the quality of this manuscript.

Appendix

List of acronyms and full names of the variables in alphabetical order

3D	Three dimensional
AB	Assawoman Bay
AI	Assateague Island
CB	Chincoteague Bay
CC	Pearson correlation coefficient
CI	Chincoteague Inlet
CO	Coastal ocean
FI	Fenwick Island
FVCOM	Finite-Volume Community Ocean Model
IWB	Isle of Wight Bay
MCBs	Maryland Coastal Bays system
NARR	North American Regional Reanalysis
NB	Newport Bay
NCEI	National Centers for Environmental Information
NDBC	National Data Buoy Center
NOAA	National Oceanic and Atmospheric Administration
NW	Northwesterly
OCI	Ocean City Inlet
MB	Mean bias
RB	Relative bias
RMSD	Root-mean square deviation
SB	Sinepuxent Bay
SWAVE	Surface wave model
USGS	United States Geological Survey
WI	Wallops Island

References

Beudin, A., Ganju, N., Defne, Z., Aretxabaleta, A.L., 2017. Physical response of a back-barrier estuary to a post-tropical cyclone. J. Geophys. Res. 122, 5888–5904.
Boynton, W.R., Murray, L., Hagy, J.D., Stokes, C., Kemp, W.M., 1996. A comparative analysis of eutrophication patterns in a temperate coastal lagoon. Estuaries 19 (2), 408–421.
Buijsman, M.C., Ridderinkhof, H., 2007. Water transport at subtidal frequencies in the Marsdiep inlet. J. Sea Res. 58 (4), 255–268.
Chen, C., Beardsley, R.C., Cowles, G., Qi, J., Lai, Z., Gao, G., Stuebe, D., Liu, H., Xu, Q., Xue, P., Ge, J., Ji, R., Hu, S., Tian, R., Huang, H., Wu, L., Lin, H., Sun, Y., Zhao, L., 2013. An Unstructured-Grid, Finite-Volume Community Ocean Model FVCOM User Manual, 3rd ed. Univ. of Mass.-Dartmouth, New Bedford, Massachusetts, p. 404. SMAST/UMASSD Tech. Rep.-13-0701.
Chen, J., Weisberg, R.H., Liu, Y., Zheng, L., 2023. Hillsborough bay inflow modification study: an application of the tampa bay coastal ocean model. Estuar. Coast. Shelf Sci. 281, 108213.
Chen, J.-L., Hsu, T.-J., Shi, F., Raubenheimer, B., Elgar, S., 2015. Hydrodynamic and sediment transport modeling of new river inlet (NC) under the interaction of tides and waves. J. Geophys. Res. 120, 4028–4047.
Cheng, R.T., Casulli, V., 1982. On lagrangian residual currents with applications in South San Francisco Bay. California. Water Resour. Res. 18 (6), 1652–1662.
Chou, Y.-J., Holleman, R.C., Fringer, O.B., Stacey, M.T., Monismith, S.G., Koseff, J.R., 2015. Three-dimensional wave-coupled hydrodynamics modelling in South San Francisco Bay. Comput. Geosci. 85, 10–21.
Cucco, A., Umgiesser, G., Ferrarin, C., Perilli, A., Canu, D.M., Solidoro, C., 2009. Eulerian and Lagrangian transport time scales of a tidal active coastal basin. Ecol. Modell. 220, 913–922.
Cuif, M., Kaplan, D.M., Lefèvre, J., Faure, V.M., Caillaud, M., Verley, P., Vigliola, L., Lett, C., 2014. Wind-induced variability in larval retention in a coral reef system: a

biophysical modelling study in the South-West Lagoon of New Caledonia. Prog. Oceanogr. 122, 105–115.
Defne, Z., Ganju, N.K., 2015. Quantifying the residence time and flushing characteristics of a shallow, back-barrier estuary: application of hydrodynamic and particle tracking models. Estuar. Coast. 38 (5), 1719–1734.
Dillow, J.J., Greene, E.A., 1999. Ground-water Discharge and Nitrate Loadings to the Coastal Bays of Maryland. U.S. Dept. of the Interior, U.S. Geological Survey.
Dodet, G., Bertin, X., Bruneau, N., Fortunato, A.B., Nahon, A., Roland, A., 2013. Wave-current interactions in a wave-dominated tidal inlet. J. Geophys. Res. 118, 1587–1605.
Donelan, M.A., F.W., Dobson, S.D., Smith, Anderson, R.J., 1993. On the dependence of sea surface roughness on wave development. J. Phys. Oceanogr. 23, 2143–2149.
Duran-Matute, M., Gerkema, T., Sassi, M.G., 2016. Quantifying the residual volume transport through a multiple-inlet system in response to wind forcing: the case of the western Dutch Wadden Sea. J. Geophys. Res. 121 (12), 8888–8903.
Fabião, J.P.F., Rodrigues, M.F.G., Fortunato, A.B., de Brito Jacob, J.M.Q., Cravo, A.M.F., 2016. Water exchanges between a multiple-inlet lagoon and the ocean: the role of forcing mechanisms. Ocean Dynam 66, 173–194.
Fairall, C.W., Bradley, E.F., Rogers, D.P., Edson, J.B., Young, G.S., 1996. Bulk parameterization of air-sea fluxes for tropical ocean-global atmosphere coupled-ocean atmosphere response experiment. J. Geophys. Res. 101 (C2), 3747–3764.
Fitzenreiter, K., Mao, M., Xia, M., 2022. Characteristics of surface currents in a shallow lagoon-inlet-coastal ocean system revealed by surface drifter observations. Estuar. Coast. https://doi.org/10.1007/s12237-022-01086-6.
Fringer, O.B., Dawson, C.N., He, R., Ralston, D.K., Zhang, Y.J., 2019. The future of coastal and estuarine modeling: findings from a workshop. Ocean Modell. 143, 101458.
Galperin, B., Kantha, L.H., Hassid, S., Rosati, A., 1988. A quasi-equilibrium turbulent energy model for geophysical flows. J. Atmos. Sci. 45 (1), 55–62.
Ganju, N.K., Suttles, S.E., Beudin, A., Nowacki, D.J., Miselis, J.L., Andrews, B.D., 2017. Quantification of storm-induced bathymetric change in a back-barrier estuary. Estuar. Coast. 40 (1), 22–36.
García-Oliva, M., Pérez-Ruzafa, Á., Umgiesser, G., McKiver, W., Ghezzo, M., De Pascalis, F., Marcos, C., 2018. Assessing the hydrodynamic response of the mar menor lagoon to dredging inlets interventions through numerical modelling. Water (Basel) 10 (7), 959.
Hasselmann, K., et al., 1973. Measurements of wind-wave growth and swell decay during the Joint North Sea Wave Project (JONSWAP). Ergänzungsheft 8–12.
Hsu, C.-Y., Kim, J., Chang, P., DiMarco, S.F., 2022. Impact of different wind representations on resonant ocean near-inertial motions in the Gulf of Mexico. Ocean Sci. J. 57, 25–36.
Hubertz, J.M., 1992. User's Guide to the Wave Information Studies (WIS) Wave Model. U.S. Army Engineer Waterways Experiment Station, Vicksburg, MS, p. 28. Version 2.0. WIS Report 27.
IAN, 2015. Coastal bays report card 2014. maryland coastal bays program, integration and application network at UMCES. https://ecoreportcard.org/site/assets/files/1792/2014-maryland-coastal-bays-report-card.pdf. Accessed 26 Sep. 2018.
Jesien, R.V., et al., 2009. Diversity of life in the coastal bays. In: Dennison, W.C., Thomas, J.E., Cain, C.J., Carruthers, T.J.B., Hall, M.R., Jesien, R.V., et al. (Eds.), Shifting Sands: Environmental and Cultural Change in Maryland's Coastal Bays. IAN Press at University of Maryland Center for Environmental Sciences, Cambridge, MD, pp. 293–344.
Kang, X., Xia, M., 2020. The study of the hurricane-induced storm surge and bay-ocean exchange using a nesting model. Estuar. Coast. 43, 1610–1624.
Kang, X., Xia, M., 2022. Stratification variability in a lagoon system in response to a passing storm. Limnol. Oceanogr. 67, 511–521.
Kang, X., Xia, M., Pitula, J., Chigbu, P., 2017. Dynamics of water and salt exchange at Maryland Coastal Bays. Estuar. Coast. Shelf Sci. 189, 1–16.
Klingbeil, K., Lamarie, F., Debreu, L., Burchard, H., 2018. The numerics of hydrostatic structured-grid coastal ocean models: state of the art and future perspectives. Ocean Modell. 125, 80–105.
Lang, G.A., Leshkevich, G.A., 2014. Persistent wind fields over the Great Lakes, 2022–2013. In: Paper presented at 57th Annual Conference on Great Lakes Research. McMaster Univ., Hamilton, Ontario, Canada, pp. 26–30. May.
Lavaud, L., Bertin, X., Martins, K., Arnaud, G., Bouin, M.-N., 2020. The construction of short-wave breaking to storm surges: the case Klaus in the Southern Bay of Biscay. Ocean Modell. 156, 101710.
Lerczak, J.A., Geyer, W.R., 2006. Mechanisms driving the time-dependent salt flux in a partially stratified estuary. J. Phys. Oceanogr. 36, 2296–2311.
Love, J.W., Chigbu, P., May, E.B., 2009. Environmental variability affects distributions of coastal fish species (Maryland). Northeast. Nat. 16 (2), 255–268.
Lu, J., Han, G., Song, D., Oliver, T., Teng, Y., Guo, J., Wu, L., Zhang, C., Jiang, X., 2021. The cross-shore component in the vertical structure of wave-induced currents and resulting offshore transport. J. Geophys. Res. Oceans 126 e2021JC017311.
Mao, M., Xia, M., 2018. Wave–current dynamics and interactions near the two inlets of a shallow lagoon–inlet–coastal ocean system under hurricane conditions. Ocean Modell. 129, 124–144.
Mao, M., Xia, M., 2020a. Monthly and episodic dynamics of summer circulation in Lake Michigan. J. Geophys. Res. 124 e2019JC015932.
Mao, M., Xia, M., 2020b. Particle dynamics in the nearshore of Lake Michigan revealed by an observation-modeling system. J. Geophys. Res. 125 e2019JC015765.
Mellor, G.L., 2003. The three-dimensional current and surface wave equations. J. Phys. Oceanogr. 33, 1978–1989.
Mellor, G.L., 2005. Some consequences of the three-dimensional current and surface wave equations. J. Phys. Oceanogr. 35 (11), 2291–2298.
Mellor, G.L., 2008. The depth-dependent current and wave interaction equations: a revision. J. Phys. Oceanogr. 38, 2587–2596.
Mellor, G.L., 2015. A combined derivation of the integrated and vertically resolved, coupled wave–current equations. J. Phys. Oceanogr. 45 (6), 1453–1463.
Mohanty, P.K., Panda, B.U.S., 2009. Circulation and mixing processes in Chilika lagoon. Indian J. Mar. Sci. 38 (2), 205–214.
Niu, Q., Xia, M., 2017. The role of wave-current interaction in Lake Erie's seasonal and episodic dynamics. J. Geophys. Res. 122 (9), 7291–7311.
Olabarrieta, M., Warner, J.C., Kumar, N., 2011. Wave-current interaction in Willapa Bay. J. Geophys. Res. 116, C12014. https://doi.org/10.1029/2011JC007387.
Ouillon, S., et al., 2010. Circulation and suspended sediment transport in a coral reef lagoon: the south-west lagoon of New Caledonia. Mar. Pollut. Bull. 61 (7–12), 269–296.
Pritchard, D.W., 1960. Salt balance and exchange rate for Chincoteague Bay. Chesapeake Sci 1 (1), 48–57.
Qi, J., Chen, C., Beardsley, R.C., Perrie, W., Cowles, G.W., Lai, Z., 2009. An unstructured-grid finite-volume surface wave model (FVCOM-SWAVE): implementation, validations and applications. Ocean Modell. 28 (1–3), 153–166.
Salas-Monreal, D., Anis, A., Salas-de-Leon, D.A., 2018. Galveston Bay dynamics under different wind conditions. Oceanologia 60 (2), 232–243.
Salles, P., Valle-Levinson, A., Sottolichio, A., Senechal, N., 2015. Wind-driven modifications to the residual circulation in an ebb-tidal delta: arcachon Lagoon, Southwestern France. J. Geophys. Res. 120 (2), 728–740.
Schwab, D.J., Morton, J.A., 1984. Estimation of overlake wind speed from overland wind speed: a comparison of three methods. J. Great Lakes Res. 10 (1), 68–72.
Smagorinsky, J., 1963. General circulation experiments with the primitive equations: I. The basic experiment. Mon. Weather Rev. 91 (3), 99–164.
Smith, N.P., 2001. Seasonal-scale transport patterns in a multi-inlet coastal lagoon. Estuar. Coast. Shelf Sci. 52 (1), 15–28.
Song, D., Wu, L., Li, Q., 2021. Effects of wave–current interactions on bay–shelf exchange. J. Phys. Oceanogr. 51 (5), 1637–1654.
Soulsby, R., 1997. Dynamics of Marine Sands. A Manual For Practical Applications. Thomas Telford Publishing, London, UK.
Tsihrintzis, V.A., Sylaios, G.K., Sidiropoulou, M., Koutrakis, E.T., 2007. Hydrodynamic modeling and management alternatives in a Mediterranean, fishery exploited, coastal lagoon. Aquacult. Eng. 36 (3), 310–324.
Umgiesser, G., Ferrarin, C., Cucco, A., De Pascalis, F., Bellafiore, D., Ghezzo, M., Bajo, M., 2014. Comparative hydrodynamics of 10 Mediterranean lagoons by means of numerical modeling. J. Geophys. Res. Oceans 119, 2212–2226.
Umgiesser, G., Zemlys, P., Erturk, A., Razinkova-Baziukas, A., Mėžinė, J., Ferrarin, C., 2016. Seasonal renewal time variability in the Curonian Lagoon caused by atmospheric and hydrographical forcing. Ocean Sci. 12 (2), 391–402.
Valle-Levinson, A., Blanco, J.L., 2004. Observations of wind influence on exchange flows in a strait of the Chilean Inland Sea. J. Mar. Res. 62, 721–741.
Valle-Levinson, A., Stanev, E., Badewien, T.H., 2018. Tidal and subtidal exchange flows at an inlet of the Wadden Sea. Estuar. Coast. Shelf Sci. 202, 270–279.
Wang, H., Wang, Z., Loftis, J.D., Teng, Y.C., 2013. Hydrodynamics and Water Quality Modeling and TMDL Development For Maryland's coastal Bays system. Final report Submitted to Maryland Department of the Environment. TMDL Technical Development Program.
Wargula, A., Raubenheimer, B., Elgar, S., Chen, J.-L., Shi, F., Traykovski, P., 2018. Tidal flow asymmetry owing to inertia and waves on an unstratified, shallow ebb shoal. J. Geophys. Res. Oceans 123, 6779–6799.
Weaver, R.J., Taeb, P., Lazarus, S., Splitt, M., Holman, B.P., Colvin, J., 2016. Sensitivity of modeled estuarine circulation to spatial and temporal resolution of input meteorological forcing of a cold frontal passage. Estuar. Coast. Shelf Sci. 183, 28–40.
Xia, M., Craig, P.M., Wallen, C.M., Stoddard, A., Mandrup-Poulsen, J., Peng, M., Schaeffer, B., Liu, Z., 2011a. Numerical simulation of salinity and dissolved oxygen at Perdido Bay and adjacent coastal ocean. J. Coast. Res. 27 (1), 73–86.
Xia, M., Xie, L., Pietrafesa, L.J., Whitney, M.M., 2011b. The ideal response of a Gulf of Mexico estuary plume to wind forcing: its connection with salt flux and a Lagrangian view. J. Geophys. Res. 116, C08035. https://doi.org/10.1029/2010JC006689.
Xu, Y., Yu, X., 2020. Enhanced formulation of wind energy input into waves in developing sea. Progr. Oceanogr. 186, 102376.
Zimmerman, J.T.F., 1979. On the Euler–Lagrange transformation and the Stokes' drift in the presence of oscillatory and residual currents. Deep Sea Res 26A, 505–520.